

Optical Domain Subsampling for Data-Efficient Optical Coherence Tomography (OCT)

by

Meena Siddiqui

B.S. Bioengineering, University of California, San Diego (2009)

Submitted to the Department of Electrical Engineering and Computer
Science

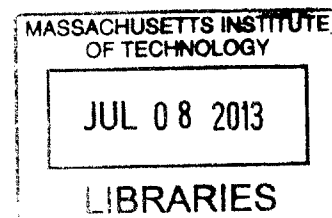
in partial fulfillment of the requirements for the degree of

Master of Science in Electrical Engineering and Computer Science

at the

MASSACHUSETTS INSTITUTE OF TECHNOLOGY

June 2013



© Massachusetts Institute of Technology 2013. All rights reserved.

Author
Department of Electrical Engineering and Computer Science
May 13, 2013

Certified by
Benjamin J. Vakoc
Assistant Professor of Health Sciences and Technology, and
Dermatology, HMS, MGH
Thesis Supervisor

Certified by
Anantha P. Chandrakasan
Professor of Electrical Engineering and Computer Science
Thesis Reader

Accepted by
/ / / Leslie A. Kolodziejski
Chairman, Department Committee on Graduate Theses

Optical Domain Subsampling for Data-Efficient Optical Coherence Tomography (OCT)

by

Meena Siddiqui

Submitted to the Department of Electrical Engineering and Computer Science
on May 13, 2013, in partial fulfillment of the
requirements for the degree of
Master of Science in Electrical Engineering and Computer Science

Abstract

Recent advances in optical coherence tomography (OCT) have led to higher-speed sources that support imaging over longer depth ranges. Limitations in the bandwidth of state-of-the-art acquisition electronics, however, prevent adoption of these advances into clinical applications. This thesis introduces optical-domain subsampling as a method for increasing the imaging range while reducing the acquisition bandwidth. Optically subsampled lasers utilize a discrete set of wavelengths to alias fringe signals along an extended depth range into a bandwidth limited window. By detecting the complex fringe signals and under the assumption of a depth-constrained signal, optical domain subsampling enables recovery of the depth-resolved scattering signal without overlapping artifacts. Key principles behind subsampled imaging will be discussed, as well as the design criteria for an experimental subsampled laser. A description of the laser, interferometer, data acquisition system, and signal processing steps is given, and the results of point spread functions compressed into a baseband window are presented. Images that were taken with the subsampled OCT system and a wide-field microscope show that this imaging scheme is viable *in vivo* and can advantageously image samples that span a long depth range.

Thesis Supervisor: Benjamin J. Vakoc

Title: Assistant Professor of Health Sciences and Technology, and Dermatology, HMS,
MGH

Acknowledgments

First, I would like to thank my advisor, Ben Vakoc, for his guidance and support throughout this research; I am very fortunate and grateful for his mentorship. I am also very glad to have crossed paths with Professor Anantha Chandrakasan in my time at MIT and thank him for all of his advice and counsel. I am happy to have had many insightful conversations and lab lunches with my labmates, Ellen, Nishant, Stephanie, Tanya, Serhat, and Isabel, and I wish them all the best in the future. This journey would have been very different without Alex and his unwavering support; thank you for your friendship and encouragement. Finally, I would like to acknowledge my family for their everlasting love and support. My parents Hafiz and Soraya, and my siblings Hadia, Harris and Madeena, and my niece Sofia have always made home feel close-by.

Contents

1	Introduction	17
1.1	Applications of OCT	17
1.2	Need for Long-Range Imaging	20
1.3	High-Speed Imaging	22
1.4	Acquisition Bandwidth Limitation	23
1.5	Thesis Organization	26
2	Theory of OCT	27
2.1	Time-Domain OCT (TD-OCT)	27
2.1.1	Low Coherence Interferometry	30
2.1.2	Scanning and Three-Dimensional Imaging	32
2.2	Fourier-Domain OCT	34
2.2.1	Sensitivity Advantage of FD-OCT	36
2.2.2	Performance Parameters of FD-OCT	38
2.2.3	Wavelength-Swept Sources	40
2.2.4	Complex-Conjugate Demodulation	44
2.2.5	Data Acquisition	47
3	Optical Subsampling in OCT	51
3.1	Relevant Work	51
3.2	Sparsity in Extended Depth Range OCT	54
3.3	Bandpass Sampling	56
3.3.1	Electrical-Domain Subsampling	58

3.3.2	Optical-Domain Subsampling	59
4	System Design and Construction	65
4.1	Optically Subsampled Laser	65
4.1.1	Laser Parameters	68
4.2	Data Acquisition	69
4.2.1	Preventing signal overlap in subsampled FD-OCT	69
4.2.2	Interferometer	71
4.3	Microscope	73
5	Performance and Imaging	75
5.1	Mirror Translation Experiment	75
5.2	Noise Analysis	77
5.2.1	Signal loss due to higher order harmonics	77
5.2.2	High frequency intensity modulation of laser	79
5.3	Signal Processing	80
5.3.1	Laser chirp in subsampled sources	82
5.4	Imaging	84
5.4.1	Finger	84
5.4.2	Rubber Phantom	87
5.5	Subsampling in Spectrometer-Based FD-OCT	88
6	Conclusion	91
6.1	Summary	91
6.2	Experimental Limitations	93
6.3	Impact of Subsampled OCT Systems	94
6.3.1	Clinical Limitations	95
6.3.2	Future Works	96

List of Figures

1-1	Representative OCT image of esophagus and corresponding histology. A & B) Normal esophagus with squamous epithelium (SE), lamina propria (LP), and muscularis mucosa (MM) clearly visible on the OCT image. C & D) Barrett's esophagus with disrupted architecture and multiple subsquamous Barrett's epithelial (SBE) glands beneath the SE [7]	18
1-2	A) Schematic of the distal optics of an OCT catheter endoscope with angled GRIN lens to minimize internal reflections. B) OCT image of rabbit trachea taken in live animal with the endoscope, and corresponding histology [28].	19
1-3	Balloon catheter centration mechanism that allows for circumferential imaging of esophagus [32]	20
1-4	(a) Endoscopic OCT image of esophagus obtained by expanding balloon. G = gland, MM = muscularis mucosa; (b) Analogous image of the duodenum where comprehensive imaging is difficult because of villi and uneven surface [25]	21
1-5	A) Longitudinal cross-sectional image of a tissue with arrows pointing to location of motion artifacts. B) Three-dimensional image of esophagus cannot be interpreted for the left 1/3 of the image [32] . .	22
1-6	Distinction between depth range and penetration depth is clear in this figure. Imaging can be performed anywhere in the depth range, however, tissue beyond the penetration depth is not imaged. The penetration depth is 2mm and depth range is 5mm in this example	25

2-1	Michelson interferometer set-up	28
2-2	(a) Fringe of a long coherence length source (b) Fringe of a short coherence length source	30
2-3	Galvanometer mirrors scan the tissue in the transverse x and y directions while translating the reference mirror	32
2-4	Focused Gaussian beam for Low NA and High NA. b = confocal parameter; r_0 = radius at minimum; D = diameter of incoming beam .	33
2-5	Simple OFDR configuration [34]	35
2-6	Schematic diagram for FDML laser; FFP-TF = tunable Fabry-Perot filter [14]	41
2-7	Swept source laser cavity with spinning polygon mirror filter [35] . . .	42
2-8	(a) polygon mirror based spectral filter [19] (b) schematic of diffraction grating where α = incident angle and β = diffraction angle	43
2-9	(A) Image segments that fall in both $+z$ and $-z$ regions overlap without complex conjugate removal (B) Image segments can be removed with conjugate demodulation [37]	44
2-10	Schematic for a frequency shifter in the reference arm [37]	45
2-11	(a) without the frequency shifter, only the positive frequency region can be used (b) with the frequency shifter both positive and negative frequency regions can be used but entire spectrum is moved to Δf [37]	46
2-12	Diagram of swept-source FD-OCT system with polarization based conjugate demodulation (dashed box). In phase (S_I) and quadrature (S_Q) signals generated with the manipulation of polarization controllers PC_I and PC_Q . Each A-line is synchronized with a TTL signal generated by a fiber-bragg grating (FBG) [31]	46
2-13	Schematic of balanced detection set-up wherein two detectors, D1 and D2, record interference fringes that are 180° out of phase. E_{SO} = input source light, E_R = electric field returning from reference arm, E_S = electric field returning from sample arm, E_{T1} = total electric field at D1, E_{T2} = total electric field at D2	47

3-1	Sample Fabry-Perot (FP) transmission spectrum; δf = instantaneous frequency, FSR = free spectral range	52
3-2	Superstructure-grating distributed Bragg reflector (SSG DBR) set-up for demonstrating discrete wavelength swept laser for OCT [2]	53
3-3	A frequency-comb FDML laser. FFP-FC = frequency comb fiber Fabry-Perot filter; FFC-TF = tunable Fabry-Perot filter; ISO = isolator; SOA = semiconductor optical amplifier [30]	55
3-4	OCT signal in an extended depth range	56
3-5	Subsampling of bandwidth limited signals. (a,b) A bandwidth limited signal sampled at twice its highest frequency content ($2f_U$) yields the full frequency content. However this is data inefficient because non-aliased sampling frequencies increase with signal frequency. (c-e) Direct subsampling of the signal at twice its bandwidth ($2B$) captures its information content by repeated aliasing of the original frequency space to the baseband window.	57
3-6	Electrical-domain subsampled receiver designs. An electrical-domain subsampling receiver (B) must retain the full RF bandwidth of the conventional fully sampled received (A), but it utilizes a lower digitization clock rate ($2B$ vs. $2F_a$). The resulting digital acquisition bandwidth is reduced by the factor of (F_a/B) and the noise is increased by the same factor (assuming white noise).	58
3-7	An illustration of wavelength evolution and fringe signals generated from a continuously wavelength swept laser (left) and an optical-domain subsampled laser source (right).	59
3-8	An optical-domain subsampling receiver can operate with lower analog bandwidth than its electrical-domain counterpart (see Figure 3-6), and can in principle eliminate the noise penalty associated with electrical-domain subsampling.	60

3-9	The ratio of the spectral bandwidth ($\Delta\lambda$) and free spectral range (FSR) determine the number of optical samples (N_S) in the laser. The instantaneous linewidth ($\delta\lambda$) can be decreased without affecting N_S in the subsampled laser	61
4-1	Sample figure of a free space wavelength swept laser with a Fabry-Perot (FP) etalon inserted in the cavity. PMF = polarization maintaining fiber; FR = Faraday rotator; BBS = broadband beam splitter; FP = Fabry-Perot; G = grating; PBS = polarization beam splitter; $\lambda/2$ = half wave plate	66
4-2	The instantaneous linewidth δf of the scanning polygon filter should be on the size scale of the FSR of the FP filter to allow smooth transition between wavelengths	67
4-3	Interference fringe signals at two depths demonstrate optical-domain generation of baseband signals. Left: lower frequency fringe corresponding to a smaller optical path difference Δl ; Right: higher frequency fringe corresponding to a larger Δl	68
4-4	The measured coherence length of the optical-domain subsampled laser incorporating an intra-cavity FP etalon exceeded 7 cm.	69
4-5	Real-valued and complex-valued signals are mapped differently into the aliased frequency space. For real-valued signals, signals located at varying locations (A) can induce distortions due to non-circular wrapping in the aliased image (B). For complex signals, wrapping is circular and overlap is avoided as long as the baseband window is large enough to contain the depth extent of the signal (C).	70
4-6	Dual channel balanced interferometer and data acquisition scheme used in subsampled imaging experiments; PBS = polarization beam splitter; BBS = broadband beam splitter; BR = balanced receiver; AOFS = acousto-optic frequency shifter; FBG = fiber-bragg grating	72

4-7	Microscope used in the subsampled OCT system. Focal length of lens =10 cm; $\theta = 30^\circ$ FOV; d = distance between galvo and sample	74
5-1	Experimental demonstration of optical-domain subsampled OCT. Interference fringes were acquired of a fixed sample while translating the reference arm mirror. The frequency content of the interference fringes demonstrates the wrapping of the mirror signal in the baseband window and presence of higher order powers.	76
5-2	Optical-domain subsampling induces a small periodic loss in baseband signal strength due to its stepwise nature and the resulting placement of signal power into higher orders. The signal variation is limited to 3.8 dB over the aliased baseband depth window. m is an integer and D_S is the baseband window depth.	78
5-3	Background signal measured with sample arm blocked. High frequency intensity modulation results from unstable wavelength transition in the subsampled laser. There were 1700 points/A-line in this measurement	80
5-4	Experimental processing flowchart	81
5-5	Laser chirping in optical-domain subsampled sources. A subsampled source can be chirped either in time (A) or k -space (B). In time, interpolation and/or k -clocking can be used to correct the nonlinearity. A nonlinear-in- k chirp, however, distorts the optical aliasing properties, and cannot trivially be corrected. Linear in k subsampled sources are a necessary technology to enable optical-domain subsampling.	83
5-6	A subsection of the <i>imagesc</i> plot of the mirror translation experiment shows the difference between chirped (top) and de-chirped (bottom) signals. The width of the PSF (indicated by high intensity red signal) is reduced while the intensity is increased when the signal is de-chirped with a re-interpolation algorithm. This process increases the axial resolution of images. A 30 dB color scale is mapped here, however, the highest true intensity could be ≥ 68 dB and the lowest ≤ 38 dB.	85

- 5-7 Cross-sectional images of a finger resting on a small breadboard, imaged with the subsampled OCT set-up. (A) Baseband window cross-section of the skin. Curvature of the sample causes wrapping of the surface at the location of the arrows. Scale bar: 500 m. (B) Tiling the baseband window (outlined in yellow) allows for continuous visualization of the sample. Arrow: fixed frequency noise resulting from laser (C) En face view of the cropped/tiled image. Bar: location of longitudinal cross section in (A). Arrow: junction between the finger and the nail. 86
- 5-8 (A) Rubber phantom resting against a metal post on a small optical breadboard. The tilted rubber phantom spans 2 cm in depth. (B) An *en face* cross section of the rubber, post, and breadboard. Aliases of the tilted rubber phantom from different depth planes into this one make it possible to visualize numerous surface reflections. (C) An *en face* cross-section from another depth results in displacement of the high intensity surface reflections (white) 89

List of Tables

1.1	Approximate Imaging Times for Various Volumes	23
1.2	Long-Range and High Speed Imaging Values	24

Chapter 1

Introduction

1.1 Applications of OCT

Optical coherence tomography (OCT) is a high-resolution, three-dimensional medical imaging modality that uses infrared laser light to probe depths within tissues [12,27]. For many applications, OCT bears advantages over other imaging modalities. With a penetration depth of a few millimeters and resolutions on the order of $5\text{ }\mu\text{m}$, it offers much deeper penetration than confocal microscopy and much higher resolution than ultrasound imaging. Furthermore, OCT provides contrast based on intrinsic index changes within the tissue, meaning that it can be administered non-invasively and without contrast agents. Because OCT images provide information about tissue microstructure, it can be used to detect pathology in various ways. In epithelial cancers, for instance, disruption of cellular organization beneath the surface of the tissue can provide indicators of dysplasia. Figure 1-1A demonstrates how the microstructure of esophageal tissue can be visualized in OCT images (panel A and C), and how disruption of the normal architecture is detected in the case of subsquamous Barrett's epithelial (panel C) [7].

Development of OCT technology began in the laboratory of James G. Fujimoto at MIT around 1991. The earliest time-domain OCT systems (TD-OCT) focused on applications in ophthalmology [12]. In 1993, the first *in vivo* tomograms of the hu-

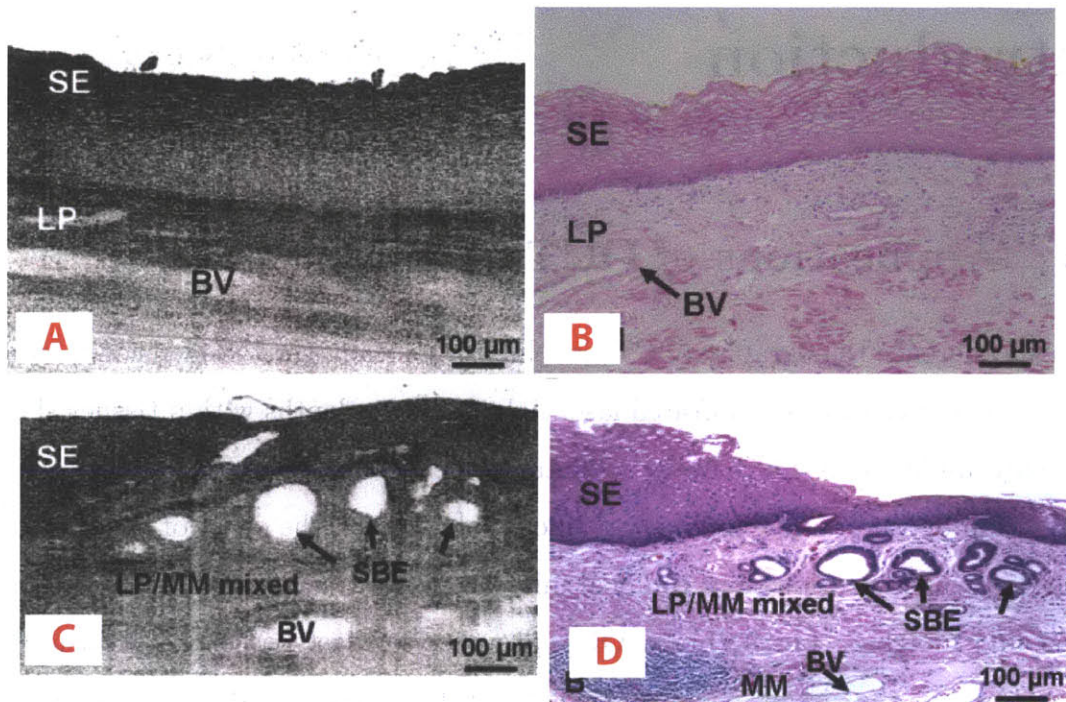


Figure 1-1: Representative OCT image of esophagus and corresponding histology. A & B) Normal esophagus with squamous epithelium (SE), lamina propria (LP), and muscularis mucosa (MM) clearly visible on the OCT image. C & D) Barrett's esophagus with disrupted architecture and multiple subsquamous Barrett's epithelial (SBE) glands beneath the SE [7]

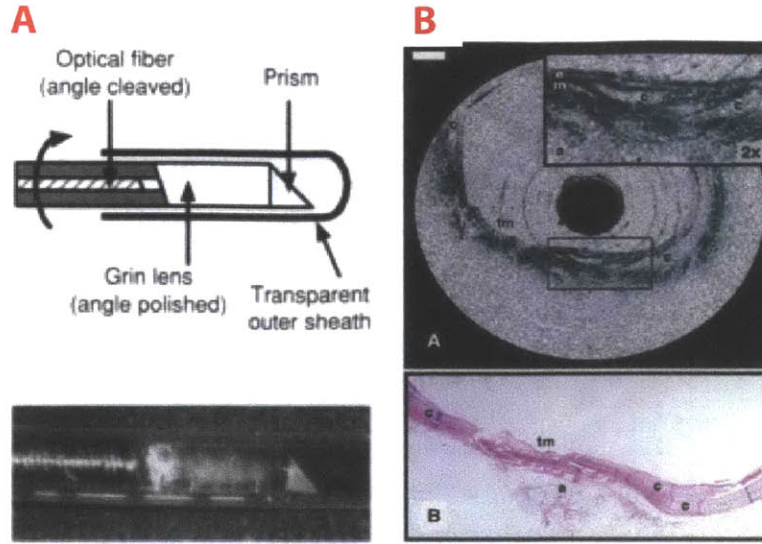


Figure 1-2: A) Schematic of the distal optics of an OCT catheter endoscope with angled GRIN lens to minimize internal reflections. B) OCT image of rabbit trachea taken in live animal with the endoscope, and corresponding histology [28].

man optic disc and macula were demonstrated [26]. With extensive research effort over the following decade, longer wavelengths and higher power lasers gave rise to imaging of optically scattering and non-transparent tissues [4]. *Ex vivo* investigation of OCT was conducted in a variety of organ systems including cartilage, gastrointestinal tissues, upper respiratory tract, and and urologic tissues [4, 16, 23, 24, 27, 28]. Initially *in vivo* imaging was only performed on external organ systems that were easy to access such as the skin, oral cavity, and eye, however, with the introduction of catheter-based fiber optic probes around 1997, imaging of internal organs became possible. Figure 1-2A shows one of the first *in vivo* catheter probes with the distal optics encased inside of a transparent housing [28].

While these first internal imaging systems were promising, they were limited in their utility due to a combination of small imaging fields, motion artifacts, and difficulty meeting geometric constraints in the organs. Nonetheless, realization of the potential of *in vivo* imaging drove research efforts in following years to focus on: 1) longer imaging ranges that reduce sensitivity roll-off due to organ geometry, 2) higher speed

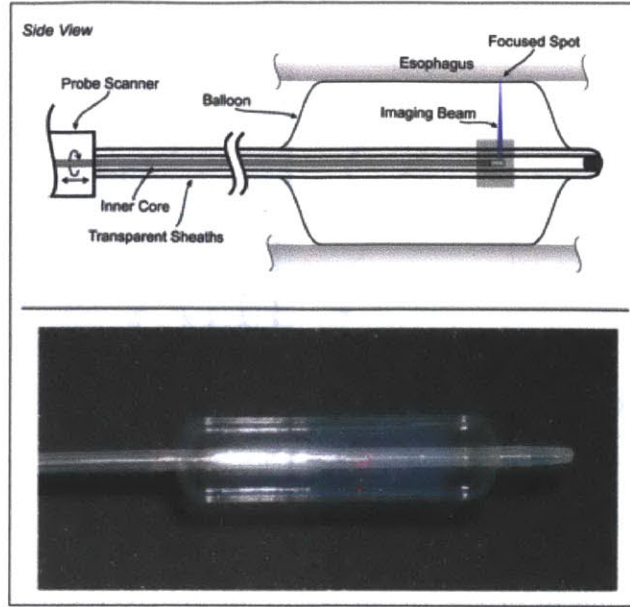


Figure 1-3: Balloon catheter centration mechanism that allows for circumferential imaging of esophagus [32]

laser sources that enable real-time image rendering and minimize motion artifacts, and 3) probe designs that facilitate comprehensive imaging of internal organs.

1.2 Need for Long-Range Imaging

The coherence length, or length over which light in a sample arm is well correlated with light in a reference arm, determines the imaging range of OCT systems [29,36]. With the current design limitations on coherence length, the location of the imaging probe relative to the tissue surface is tightly constrained (to within ~ 5 mm). If the tissue is located more than a few millimeters from its ideal location, the OCT system rapidly loses image contrast due to low sensitivity beyond this region. Thus, for OCT to work, the geometry must be arranged to ensure millimeter-level control of the probe-to-tissue distance. In the esophagus, the smooth and tubular nature of the organ allows imaging through a balloon-centration catheter (Figure 1-3) [32]. In this special case, the catheter is inserted into the esophagus and the balloon stretches the wall of the esophagus so that it is a constant distance around the central imaging

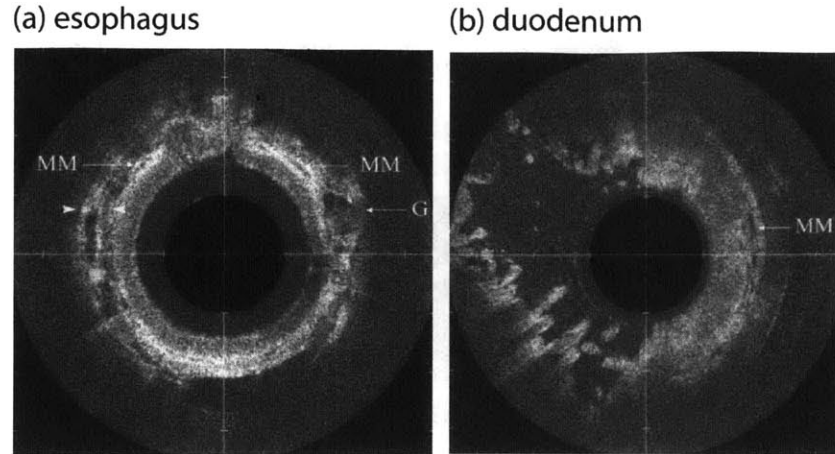


Figure 1-4: (a) Endoscopic OCT image of esophagus obtained by expanding balloon. G = gland, MM = muscularis mucosa; (b) Analogous image of the duodenum where comprehensive imaging is difficult because of villi and uneven surface [25]

catheter. This ensures that the geometric constraints described above can be met; with pull-back of the core catheter, comprehensive imaging of the esophagus can be performed over the length of the balloon (Figure 1-4a) [25]. Analogous catheters cannot be easily created for other organs that have more complex geometry. For instance, because tissue along the intestines are have irregular crypts and varying diameters at different sections, balloon catheterization is not as effective in centering the imaging probe. Figure 1-4b shows a cross-section of the duodenum that is imaged with the same balloon catheter as the esophagus, and it demonstrates the difficulty of getting comprehensive imaging in the same way as for the esophagus. The left side of the duodenum has fallen beyond the imaging range of the system and has not been imaged properly. Thus, unless the organ meets specific geometric criteria, no solution exists to constrain the probe-to-tissue distance in order to stably image the organ system. OCT lasers that increase coherence length (and thus sensitivity over longer ranges) have been investigated by various groups. As new laser sources are demonstrated with multi-cm scale coherence lengths [22], new clinical and industrial applications of OCT based on simultaneous high-speed and multi-cm depth ranges can be envisioned.

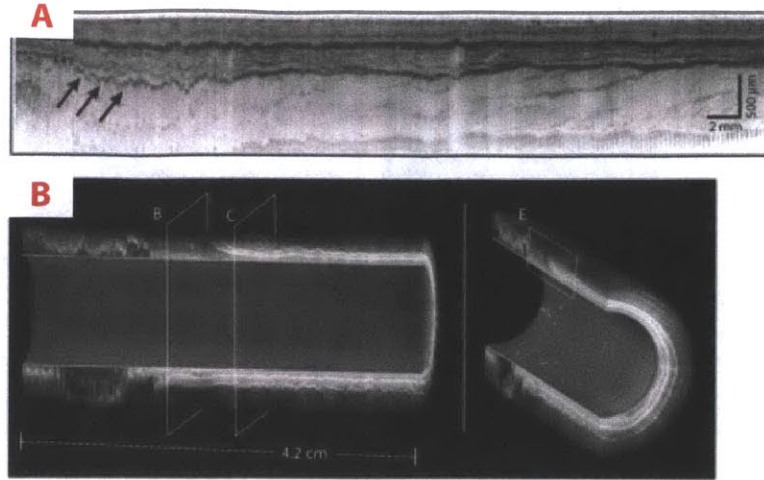


Figure 1-5: A) Longitudinal cross-sectional image of a tissue with arrows pointing to location of motion artifacts. B) Three-dimensional image of esophagus cannot be interpreted for the left 1/3 of the image [32]

1.3 High-Speed Imaging

High-speed imaging is important for minimizing motion artifacts during the imaging session as well as for real-time image rendering. Most tissues in the body do not remain stable for prolonged periods of time, and are subject to various motions whether from breathing, heart beating, peristalsis, or other biological functions. Significant motion of the tissue relative to the imaging probe within this time induces artifacts in the image that are difficult to remove in the processing stage (Figure 1-5a). To minimize these artifacts, tissue must be immobilized for the duration of the imaging session; while this is straightforward in external tissues, it poses a larger challenge in internal organs. In the esophagus, the aforementioned balloon catheter provides stabilization to limit motion during the imaging procedure, however, some motion is unavoidable even in these applications (Figure 1-5b) [32]. Furthermore, as mentioned before, stabilization via a balloon catheter cannot be applied to many other internal organs, and as such motion artifacts are prohibitively large.

Alternatively, motion artifacts can be minimized by increasing the speed of imaging. In OCT, the A-line rate (given in Hz) is the number of axial scans that can

Table 1.1: Approximate Imaging Times for Various Volumes

A-line Rate	1cm x 1cm x 2mm	5cm x 5cm x 2mm
1 kHz	1.1 hours	27 hours
100 kHz	6 mins	2.7 hours
1 MHz	4 s	1.7 mins
10 MHz	0.4 s	10 s

be completed in one second. The faster the A-line rate, the faster one depth scan is acquired and thus less motion can occur during that interval. Table 1.1 provides some reference values for the time it takes to acquire a 1cm x 1cm x 2mm or a 5cm x 5cm x 2mm volume at different A-line rates. Ideally, imaging of the area of interest would be performed in less than one second since cardiac motion occurs on an average of once per second.

The first generation TD-OCT systems relied on a translating reference arm for depth scanning and only operated at a few kHz. Consequently, motion artifacts were severe and imaging could only reliably be performed on small volumes [12, 16, 23]. The introduction of Fourier-domain OCT (FD-OCT) obviated the need for a translating reference arm and instead relied on the laser source for imaging speed. In 2004, swept-wavelength OCT imaging was demonstrated at 100 kHz A-line rates [34]. Since that time, multiple new swept-wavelength technologies have been developed and laser speeds have increased to the order of MHz [14, 20]. With this increase in speed, *in vivo* imaging is becoming easier and more informative.

1.4 Acquisition Bandwidth Limitation

The bandwidth of the electronic acquisition systems used to capture OCT signals has increased through adoption of higher-speed digitizers and higher bandwidth bus interfaces. When the requirements of high-speed are combined with those of extended depth range imaging, however, current acquisition electronics are unable to accom-

Table 1.2: Long-Range and High Speed Imaging Values

Parameter	Standard	Long-Range	High-Speed	Long-Range + High-Speed
Laser Speed	100 kHz	100 kHz	1.2 MHz	1.2 MHz
Axial Imaging Range	5 mm	10 cm	5 mm	10 cm
Acquisition Bandwidth	200 MS/s	4 MS/s	2.4 GS/s	48 GS/s

moderate the resulting signal bandwidth. In OCT, the required acquisition bandwidth scales with the product of the laser speed and imaging depth range. Table 1.2 shows some example values of laser speed, imaging range, and expected acquisition bandwidth for different combinations of OCT parameters. The combination of long range and high speed imaging results in 48 GSamples/s, which is well beyond what modern digitizer cards are able to acquire. In this work, we demonstrate a method to dramatically reduce the acquisition bandwidth required for extended depth range imaging, and thereby enabling high-speed and extended depth range OCT with current acquisition electronics.

The distinction between the imaging range/depth range and the penetration depth into tissue should be highlighted (Figure 1-6). The penetration depth of light into tissue refers to how far into the tissue light can travel, and thus how far into the tissue OCT images can be obtained. This depth depends on the wavelength of the light, the power of the light source, and the tissue being imaged. Typically for non-transparent tissues such as skin or esophagus, penetration depths are $\sim 2\text{mm}$. On the other hand, the depth range of imaging refers to the region in which the tissue must be placed in order for it to be within the high-sensitivity region of the system. This range depends on the coherence length of light, which relies on the instantaneous linewidth of the laser as will be discussed in section 2.2. In this work, we provide a technique to increase the depth range of imaging, Δz , without increasing the acquisition bandwidth. Our approach is based on modifying the optical sampling approach in OCT so that wavelengths are discretely instead of continuously sampled. Frequency comb lasers

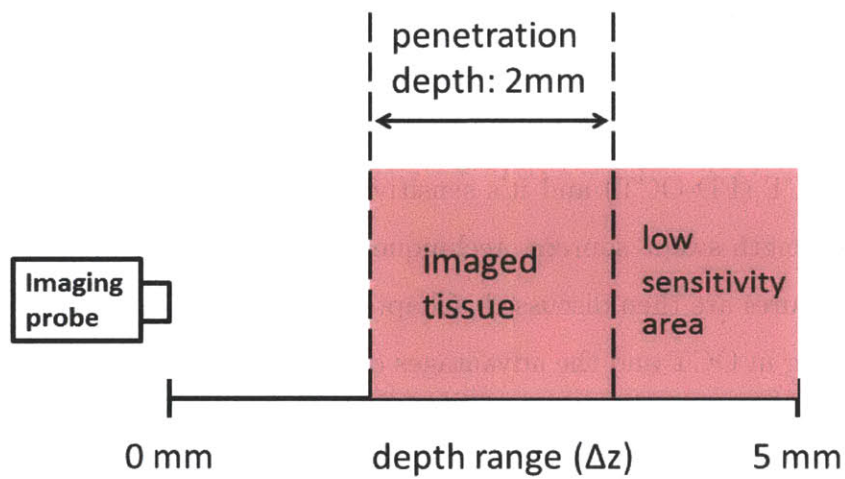


Figure 1-6: Distinction between depth range and penetration depth is clear in this figure. Imaging can be performed anywhere in the depth range, however, tissue beyond the penetration depth is not imaged. The penetration depth is 2mm and depth range is 5mm in this example

have been demonstrated previously to extend the coherence length of source or reduce fringe decay (reviewed in section 3.1), but until now has not been demonstrated as a method for data-compressive ranging.

1.5 Thesis Organization

The goal of this work was to provide a robust proof of concept for applying subsampling to provide data efficient depth ranging in OCT. Chapter 2 describes some salient OCT concepts that were utilized extensively in this work. A brief introduction to interferometry and time-domain OCT (TD-OCT) is given followed by a discussion of fourier-domain OCT (FD-OCT) and it's sensitivity advantage over TD-OCT. Some designs for wavelength-swept sources, techniques for conjugate demodulation, and acquisition procedures are then discussed. Chapter 3 discusses the theory behind applying subsampling in OCT and the advantages of using optical-domain subsampling over electrical-domain subsampling. Chapter 4 details the design of a preliminary swept frequency comb laser, the interferometer, and microscope for imaging. Key performance attributes of optical subsampling are highlighted. Finally, Chapter 5 presents the preliminary imaging results of the optically subsampled OCT system.

Chapter 2

Theory of OCT

The fundamental structure of OCT systems consists of three major components: a light source, an interferometer, and a data acquisition/processing unit. At the core of OCT theory is the concept of light interferometry. This chapter begins by introducing the the concept of interferometry in the context of time-domain OCT (TD-OCT). The evolution of OCT into the Fourier-domain is then described as well as some prevailing concepts that this work is built upon, including removal of complex ambiguity from OCT interference signals, and acquisition with balanced detectors.

2.1 Time-Domain OCT (TD-OCT)

The Michelson interferometer was first introduced Albert Abraham Michelson around 1881 and has been invaluable in the field of optics since. It is prevalent today for various applications including precision measurements, space research, and communications. In OCT, the Michelson interferometer is employed as a tool to indirectly measure backscattered light from different depths within a sample; this backscattered light coming from different depths is otherwise traveling too fast for modern photodetectors to acquire. A common schematic of this interferometer is shown in Figure 2-1. Light that is generated from a source enters the beam splitter (BS) from the left and is divided into the reference arm and the sample arm. The light that is backreflected from each arm recombines at the beam splitter and the interference of

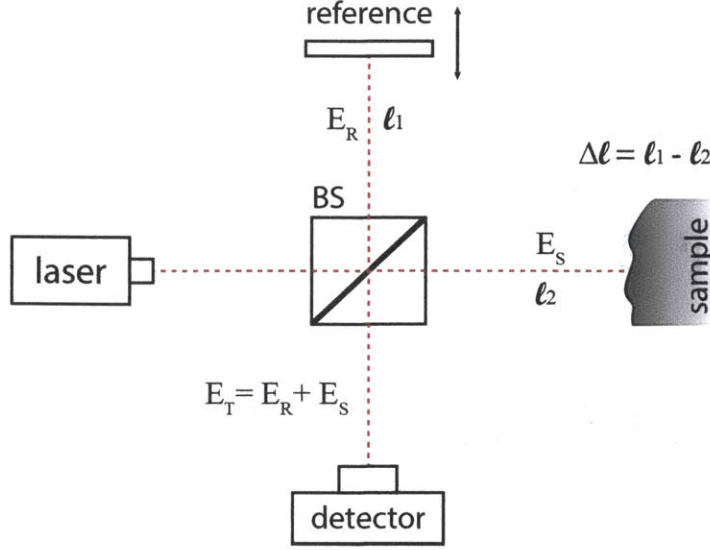


Figure 2-1: Michelson interferometer set-up

these two beams is received by a photodetector. Consider the simplest case where the light being supplied by the laser is purely monochromatic with wavenumber k and that the sample is a 100% reflective mirror. The electric field of the light in the reference arm is $E_R e^{jkl_1}$ and in the sample arm $E_S e^{jkl_2}$. When the light recombines at the beam splitter the total electric field is the superposition of these electric fields (assuming the system is linear) [10]:

$$E_T = E_S + E_R = E_R e^{2jkl_1} + E_S e^{2jkl_2} \quad (2.1)$$

where the factor of 2 results from the fact that the light experiences double-pass in each arm. For simplicity, the phase delays induced by the components in the optical beam path are ignored and will be addressed in section 2.2.5. Because photodetectors detect the irradiance (energy per unit area per unit time) rather than the electric field, this interference term needs to be expressed in terms of irradiance [10],

$$I \equiv \langle S \rangle_T = \frac{\epsilon \nu}{2} \langle |E_T|^2 \rangle \quad (2.2)$$

where S is the magnitude of the Poynting vector, ν is the speed of the wave in the medium, ϵ is the permittivity, and $|E_T|$ is the magnitude of the total electric field. The square of the magnitude of the total electric field can be equivalently written as [5, 10],

$$\begin{aligned}
E_T^2 &= E_T E_T^* = (E_S + E_R)(E_S + E_R)^* \\
&= (|E_R|e^{2jkl_1} + |E_S|e^{2jkl_2})(|E_R|e^{-2jkl_1} + |E_S|e^{-2jkl_2}) \\
&= |E_R|^2 + |E_S|^2 + |E_R||E_S|(e^{2jk(l_1-l_2)} + e^{-2jk(l_1-l_2)}) \\
&= |E_R|^2 + |E_S|^2 + 2|E_R||E_S|\cos(2k\Delta l)
\end{aligned} \tag{2.3}$$

where Δl refers to the optical path difference between the sample and the reference arm as shown in Figure 2-1. The irradiance can be expressed as [5],

$$I = \frac{\epsilon\nu}{2}(|E_R|^2 + |E_S|^2 + 2|E_R||E_S|\cos(2k\Delta l)) \tag{2.4}$$

The first two terms correspond to the DC components of the irradiance and are ignored or subtracted. The last term corresponds is the cross-correlation term and says that the irradiance, I , varies sinusoidally with optical path difference Δl . Thus if the reference mirror is scanned back and forth in time, t , then the detector current varies sinusoidally in time as well. This current is often expressed as [4, 5],

$$i_{det}(t) = \frac{\eta q}{h\nu}(|E_R|^2 + |E_S|^2 + 2|E_R||E_S|\cos(2k\Delta l(t))) \tag{2.5}$$

where η is the quantum efficiency of the detector, q is the quantum electric charge (1.6×10^{-19}), and $h\nu$ is the photon energy. Notice that the amplitude of the signal is proportional to the product of the magnitude of the reference and sample electric fields, implying that a weak backscattered field from the sample can be amplified by mixing with a strong reference field.

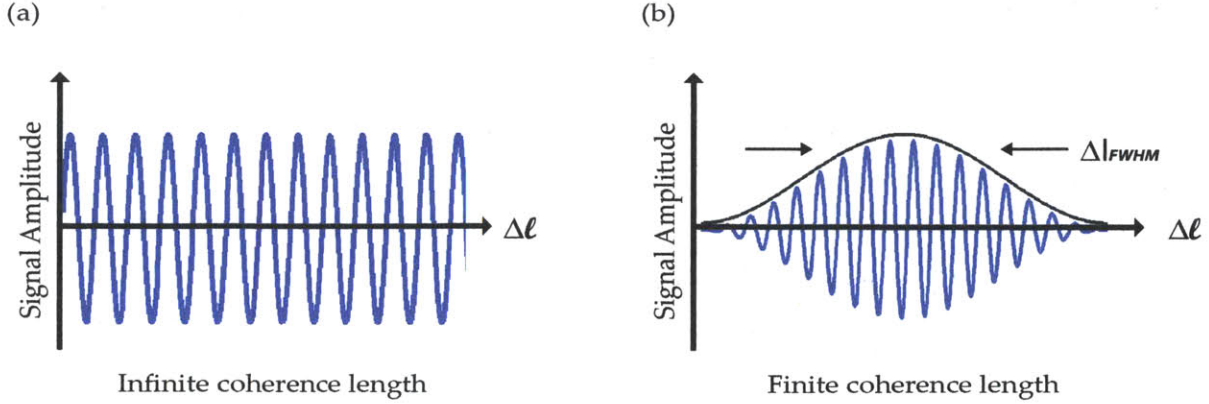


Figure 2-2: (a) Fringe of a long coherence length source (b) Fringe of a short coherence length source

2.1.1 Low Coherence Interferometry

Because of the assumption of monochromatic light source in the previous derivation, the source has infinite coherence and a fringe produced from such a system would be infinitely periodic (Figure 2-2a). In the case where light with a broad spectral bandwidth is used, however, the fringe decays to the noise floor and has a finite duration (Figure 2-2b). As predicted by the Heisenberg Uncertainty Principle, there is an inverse relationship between the spectral bandwidth, Δf , of the source and the pulse duration in the time domain, termed the coherence time (Δt_c). The length of this envelope in free space is defined as the coherence length and is given by [10],

$$\Delta l_c = c\Delta t_c \quad (2.6)$$

where $c = 3 \times 10^8$ m/s. In this case of low coherence, the expression for electric fields in the sample and reference arms are no longer simple monochromatic expressions but rather a function of frequency [4, 5, 10]:

$$\begin{aligned} E_R(\omega) &= |E_R|e^{-j[2B_R(\omega)l_1 - \omega t]} \\ E_S(\omega) &= |E_S|e^{-j[2B_S(\omega)l_2 - \omega t]} \end{aligned} \quad (2.7)$$

where B_R and B_S are propagation constants for reference and sample fields respectively. This time, the interference term is proportional to the sum of interference terms from each individual ω in the wave packet [4, 5, 10],

$$\begin{aligned} i_{det} &\propto \text{real}\left\{\frac{1}{2\pi} \int_{-\infty}^{\infty} E_S(\omega) E_R(\omega)^* d\omega\right\} \\ &\propto \text{real}\left\{\frac{1}{2\pi} \int_{-\infty}^{\infty} S(\omega) e^{-2j\Delta l(B_S(\omega) - B_R(\omega))} d\omega\right\} \end{aligned} \quad (2.8)$$

where $S(\omega)$ is the power spectrum of the source. For the case of uniform, linear, and nondispersive material in both the sample and reference arms, B can be considered equal in each arm of the interferometer and it can be assumed that phase mismatch is solely dependent on the pathlength difference, Δl . The detector current becomes [5],

$$i_{det} \propto \text{real}\left\{e^{-j\omega_0\Delta\tau_p} \frac{1}{2\pi} \int_{-\infty}^{\infty} S(\omega - \omega_0) e^{-j(\omega - \omega_0)\Delta\tau_g} d(\omega - \omega_0)\right\} \quad (2.9)$$

where ω_0 is the center frequency of the source spectrum, $\Delta\tau_p$ is the phase delay, $\Delta\tau_g$ is the group delay. It is easy to see now that the equation contains two oscillatory terms. The first exponential function is the rapid oscillations resulting from phase modulation while the second exponential function is the slower oscillation corresponding to the envelope shown in Figure 2-2b (which is Gaussian in shape, reflecting a Gaussian source). This latter term is an autocorrelation function and is the inverse Fourier transform of the source power spectrum as per the Wiener-Kinchine theorem [5, 23]. Because of this Fourier transform relationship, larger spectral bandwidths result in narrower envelopes and vica versa. It is noteworthy that the source must ideally have a Gaussian frequency spectrum so that the autocorrelation function is also Gaussian and high axial resolutions (δz) can be obtained [4]. The width of this envelope at it's full-width-half-max (FWHM) is proportional to the coherence length, Δl_c , and for a Gaussian source is given by,

$$\Delta l_c = \frac{2\ln 2}{n\pi} \frac{\lambda_0^2}{\Delta\lambda} \quad (2.10)$$

where λ_0 is the center wavelength, $\Delta\lambda$ is the spectral bandwidth and n is the refractive index of the sample [4]. The width of the autocorrelation function also determines

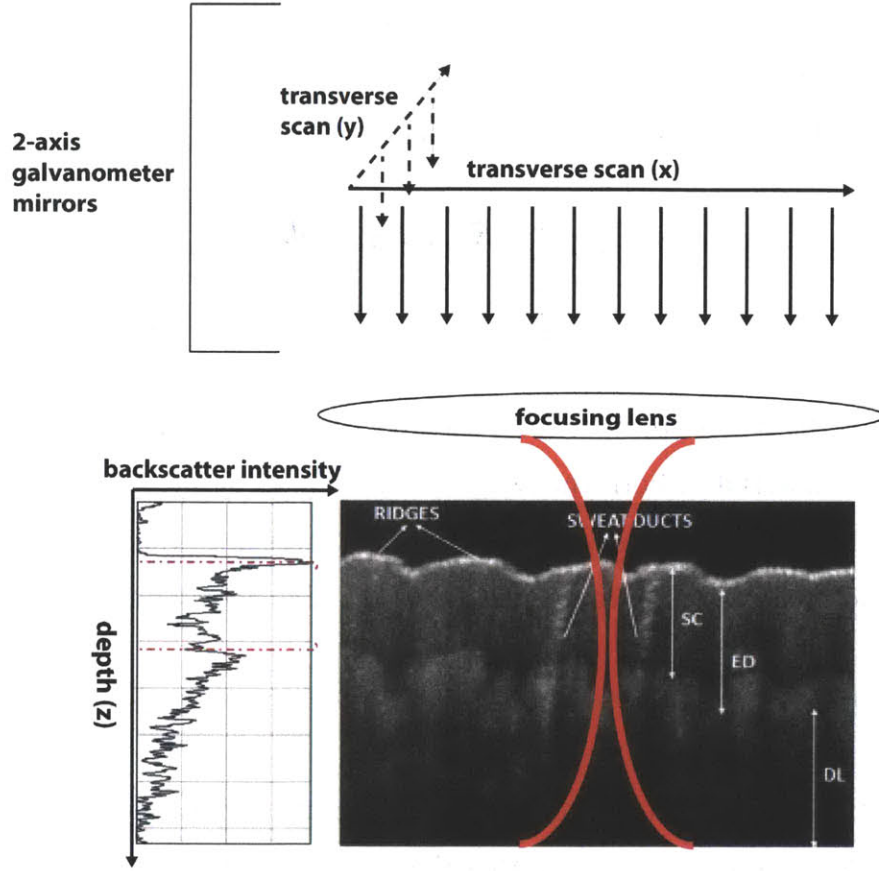


Figure 2-3: Galvanometer mirrors scan the tissue in the transverse x and y directions while translating the reference mirror

the axial resolution, $\delta z = \Delta l_c$ of the OCT system, thus broadband sources are used in OCT to maximize this resolution.

2.1.2 Scanning and Three-Dimensional Imaging

Three-dimensional imaging in OCT is obtained by scanning the tissue in all three spatial axis. In the case of depth scan (z direction in Figure 2-3) the reference mirror is translated to obtain backscatter intensity information from different depths within the tissue; this is known as the A-line or A-scan. Two galvanometer mirrors rotate in the x and y directions to provide scanning in the transverse direction; this is known as the B-scan and C-scan. As in conventional microscopy, a lens focuses the collimated light coming from the galvanometer mirrors into the tissue. Unlike the

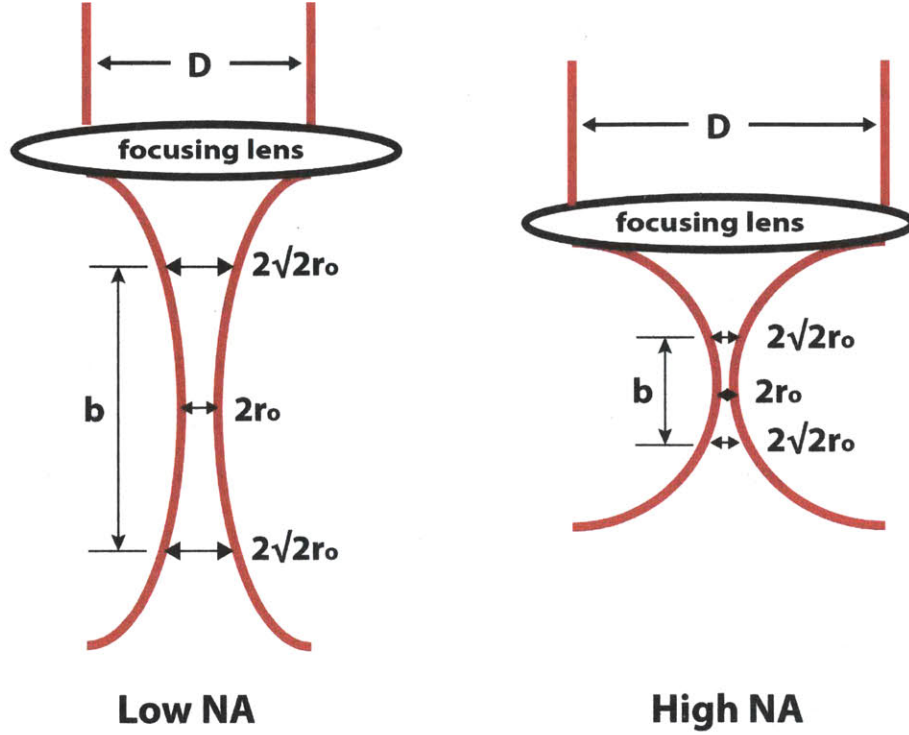


Figure 2-4: Focused Gaussian beam for Low NA and High NA. b = confocal parameter; r_0 = radius at minimum; D = diameter of incoming beam

axial resolution, which was determined by the low coherence gate of the light source as given by equation 2.28, transverse resolution is determined by the focusing optics in the microscope. Assuming a Gaussian beam profile (the field amplitude in the transverse direction has a Gaussian distribution), the minimum spot size ($\frac{1}{e^2}$ width) can be calculated by [4],

$$\delta x = \delta y = \frac{4\lambda}{\pi} \frac{f}{D} \quad (2.11)$$

where f is the focal length of the lens, λ is the wavelength of the beam, and D is the diameter of the beam that enters the focusing lens. Thus the larger the numerical aperture ($NA \propto \frac{D}{2f}$) of the beam, the the higher the transverse resolution at the minimum waist spot (Figure 2-4). However, because the penetration of OCT light into tissue is typically on the order of 2 mm, low numerical apertures are needed in order to increase the confocal parameter so that the whole depth of the tissue being imaged is in relatively good focus. The confocal parameter, b , is twice the Raleigh

length and denotes the range over which the beam waist expands to $\sqrt{2}r_0$. The confocal parameter for a Gaussian beam is given by the following relation [4],

$$b = \frac{\pi(\delta x)^2}{2\lambda} \quad (2.12)$$

In some applications higher NA can be used to provide ultra-high transverse resolutions at the expense of depth-of-field. Some microscopes with adjustable focus have been explored as alternatives ways to have very high transverse resolution while maintaining large field depths, however as long as the field depth remains small, the transverse resolution generally suffices and many elect to avoid the complexity of adjustable focus microscopes [11].

2.2 Fourier-Domain OCT

The transition from time-domain OCT (TD-OCT) to frequency domain (FD-OCT) followed closely from the development of optical frequency domain reflectometry (OFDR). This major technological advancement for OCT imaging gave way to improved detection sensitivity. It was also the first step toward significant progress in imaging speed in following years because a physically scanning reference mirror was no longer required. The basic configuration of an OFDR system is shown in Figure 2-5 [34]. In this embodiment of OFDR, light from a tunable source splits 50/50 by a fiber beam splitter into the reference and the sample arm. Light that is backreflected from each arm interfer at the beam splitter and is detected with a photodetector. This time the reference mirror remains stationary while the wavelengths are swept in time, $k(t)$. The detector current analogous to equation 2.5 for a reference mirror at $\Delta l = z_0$ now becomes [4, 5, 34],

$$i_{det}(t) \propto r(z_0) \frac{\eta q}{h\nu} (2|E_R| |E_S| \cos(2k(t)z_0)) \quad (2.13)$$

where again ν is the quantum efficiency of the detector, q is the quantum electric charge, $h\nu$ is the photon energy, and $r(z_0)$ is the reflectivity of the sample as a function

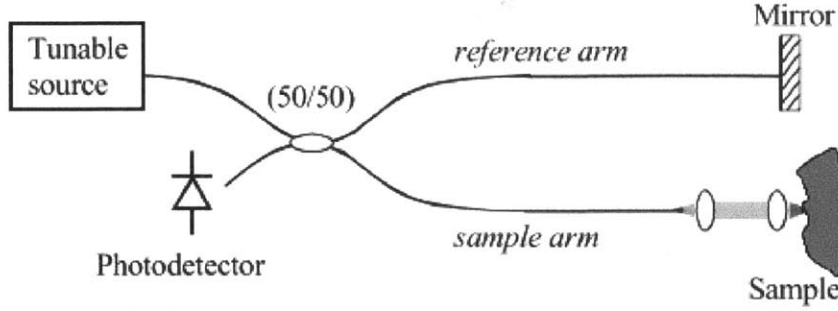


Figure 2-5: Simple OFDR configuration [34]

of depth. If the wavenumber, $k(t)$ is varied linearly in time with a slope α then $k(t) = k_i + \alpha t$ where k_i is the lowest wavenumber in the spectral profile. And the signal current becomes [34],

$$i_{det}(t) \propto r(z_0) \frac{\eta q}{h\nu} (2|E_R| |E_S| \cos(2(k_i + \alpha t)z_0)) \quad (2.14)$$

The detector current is proportional to the reflectivity of the sample at each depth, $r(z_0)$, and the instantaneous frequency of the signal ($f_{sig} = \frac{\alpha}{\pi} z_0$) encodes the depth (z_0). Through a simple discrete fourier transform (DFT), the reflectivity profile of the sample at the optical path delay, z_0 can be obtained. The complete expression for detector current for the case where the sample is not a single reflector, but a partially transparent tissue sample is [34],

$$i_{det}(t) = \frac{\eta q}{h\nu} (P_r + P_0 \int r^2(z) dz + 2\sqrt{P_r P_0} \int r(z) \Gamma(z) \cos(2k(t)z + \phi(z)) dz) \quad (2.15)$$

where P_r is the optical power reflected from the reference arm, P_0 is the optical power illuminating the sample, $\Gamma(z)$ is the coherence function, $\phi(z)$ is the phase of the reflectance profile of the sample, and again $r(z)$ is the reflectivity at depth z .

2.2.1 Sensitivity Advantage of FD-OCT

A primary goal in OCT is to have a shot-noise-limited system. There are four dominant sources of noise in OCT systems: thermal noise arises from the exchange of thermal energy from passive electrical components such as resistors within the system; shot noise is the consequence of the quantized nature of light and charge and is proportional to the quantum electric charge, e , and the $\sqrt{\text{photocurrent power}}$; RIN describes any noise source whose power spectral density scales linearly with the mean photocurrent power; and finally, amplified spontaneous emission noise refers primarily to noise generated in the data acquisition board [4]. While the other sources of noise can be minimized by high-gain electrical amplification, selecting appropriate reference arm power, and/or using dual-balanced detection as discussed later in section 2.2.5, shot noise is fundamental to the detection of the optical interference fringes. In this shot noise limit, FD-OCT has a significant advantage over TD-OCT. In OCT, sensitivity is defined as the minimum reflectivity that produces signal power equal to the noise power, or when the signal-to-noise ratio (SNR) is equal to one,

$$SNR = \frac{\langle i_s^2(t) \rangle}{\langle i_n^2(t) \rangle} = 1 \quad (2.16)$$

where brackets $\langle \rangle$ denote time average. For a shot-noise-limited TD system, the signal-to-noise ratio has been shown to be [4],

$$SNR_{TD} = \frac{\eta P_s}{2h\nu(NEB)} \quad (2.17)$$

where again η is the quantum efficiency of the photodetector, $h\nu$ is the photon energy, NEB is the noise-equivalent-bandwidth of the system, and P_s is the power backreflected from the sample arm. The NEB is the detection bandwidth and is proportional to the A-line rate of the laser (f_A) and the spectral bandwidth ($\Delta\lambda$) [4].

$$NEB \propto f_A \Delta\lambda \quad (2.18)$$

As shown earlier in equation 2.28, the axial resolution of TD-OCT, δz is inversely proportional to the spectral bandwidth of the source. Thus [4],

$$NEB \propto \frac{f_A}{\delta z} \quad (2.19)$$

This implies that the TD sensitivity is directly proportional to optical power and axial resolution and inversely proportional to imaging speed [4],

$$SNR_{TD} \propto \frac{\eta P_s \delta z}{2h\nu f_A} \quad (2.20)$$

This tradeoff between these three important parameters ultimately limits the performance of TD-OCT systems. Conversely, in FD-OCT, there is no tradeoff between axial resolution and imaging speed, offering a significant advantage in imaging speed.

Recall that the reflectivity profile $r(z)$ can be obtained via a Fourier Transform. Assuming that there are N_S samples within the spectral bandwidth, $\Delta\lambda$, then the sequence of N_S complex numbers is transformed into an N_S -periodic sequence of complex numbers according to the DFT formula [6, 18, 34]:

$$F_S(z_l) = \sum_{m=0}^{N_S-1} i(k_m) e^{-j2\pi l m / N_S} \quad (2.21)$$

Thus the absolute square of the peak value of F_S is proportional to the reflectivity. Furthermore, because of Parseval's theorem $\sum F^2 = N_S \sum i^2$, the noise power level in the Fourier domain is given by $\langle F_n^2 \rangle = N_S \langle i_n^2 \rangle$ while the signal power F_S^2 is zero except at $z_l = \pm z_0$. Thus at each of the peaks, the power is [34],

$$|F_S(z_l = +z_0)|^2 = 0.5 N_S \sum i_s^2 = \frac{N_S^2}{2} \langle i_s^2 \rangle \quad (2.22)$$

Therefore,

$$SNR_{FD} = \frac{|F_S(z_l = +z_0)|^2}{\langle F_n^2 \rangle} = \frac{N_S}{2} SNR_{TD} \quad (2.23)$$

Thus while the noise power is distributed across all frequencies, the signal power is concentrated at two peak with frequencies corresponding to a specific depth in the sample ($\pm z_0$) [6]. Note that this relies on noise currents that are mutually uncorrelated and thus relies on white noise powers adding incoherently. Although this is derived assuming a square-profile spectral envelope and 100% tuning duty cycle, it is shown that equation 2.23 is valid for more general cases of Gaussian spectral profile and less than 100% tuning duty cycle. In the shot noise limit, the signal-to-noise ratio of the FD-OCT signal can be approximated as [34],

$$SNR_{FD} \propto \frac{\eta P_s}{h\nu f_A} \quad (2.24)$$

remembering that N_S is proportional to the spectral bandwidth, $\Delta\lambda$, of the laser source. Comparing equation 2.20 to equation 2.24, it becomes apparent that the noise-equivalent-bandwidth (*NEB*) of FD-OCT is proportional only to the speed of the laser (A-line rate) rather than the product of the laser speed and spectral bandwidth. Therefore, there is a significant sensitivity advantage of FD-OCT over TD-OCT and most modern OCT system employ this newer approach.

2.2.2 Performance Parameters of FD-OCT

The performance of FD-OCT relies more heavily on the specifications of the light source than TD-OCT. Because depth scanning is now performed by tuning wavelengths in the laser rather than translating the reference arm, the A-line rate, f_A , is equivalent to the speed of wavelength tuning in the laser. Furthermore, since the reference mirror remains stationary, the optical path difference, Δl , is constant and does not vary as a function of time as in equation 2.5. As a result, the ranging depth of FD-OCT systems is determined by the instantaneous linewidth of the swept wavelengths, $\delta\lambda$, in the laser. This instantaneous linewidth is the finite bandwidth of the individual wavelengths and defines the coherence length of the laser, or the optical path difference over which the light in the sample and reference arms are well correlated with one another. Thus the region over which imaging can be performed

with good sensitivity and is analogous to the ranging depth, Δz , which is given by the equation [4, 34],

$$\Delta z = \frac{\lambda_0^2}{4n\delta\lambda} \quad (2.25)$$

where again λ_0 is the center wavelength, and n is the index of refraction of the sample arm. The instantaneous linewidth, $\delta\lambda$, should not be confused with the spectral bandwidth, $\Delta\lambda$ which is the overall bandwidth of the broadband source. In fact, the ratio of these two values determines the number of optical samples, N_S , within this broadband profile [4]:

$$N_S = \frac{\Delta\lambda}{\delta\lambda} \quad (2.26)$$

Recall from equation 2.21 that this leads to an N_S -periodic DFT. As long as the samples per axial scan of the OCT system is greater than N_S , the amplitude of the coherence function, $\Gamma(z)$, will not decay with depth, z , and full usable imaging range can be utilized. Assuming this to be the case, then the acquisition bandwidth, BW , of continuous FD-OCT sources can be approximated as [4],

$$BW = N_S f_A = \frac{\Delta\lambda}{\delta\lambda} f_A \quad (2.27)$$

It is now quantitatively confirmed that the acquisition bandwidth increases proportionally as both imaging speed (f_A) and ranging depth ($\propto \frac{1}{\delta\lambda}$) increase (Table 1.2 has already suggested this in section 1.4). Since the acquisition bandwidth is limited by the bandwidth of modern digitizer cards, it is clear now that there is a tradeoff between imaging speed, ranging depth, and axial resolution. As will be discussed later in section 3.3.2, optical subsampling can relieve this limitation by decoupling the ranging depth from this expression so that the ranging depth can be increased without increasing acquisition bandwidth.

Similar to TD-OCT, the axial resolution in FD-OCT is given by the expression [34],

$$\delta z = \frac{2\ln 2}{n\pi} \frac{\lambda_0^2}{\Delta\lambda} \quad (2.28)$$

where $\Delta\lambda$ is the spectral bandwidth and n is the refractive index of the sample. Thus, axial resolution, δz , is still determined by the spectral bandwidth of the source and should be maximized.

2.2.3 Wavelength-Swept Sources

The major considerations for the light source include center wavelength, spectral bandwidth, coherence length, output power, and sweep repetition rate (A-line rate). The penetration depth of light into tissue is limited by absorption and scattering, which are both wavelength dependent phenomenon. Thus, the center wavelength of OCT sources are chosen at locations where the balance of absorption and scatter maximize penetration of light into the tissue, mainly at 850nm, 1300nm, or 1550nm [4]. To maximize spectral bandwidth, $\Delta\lambda$, and axial resolution, broadband semiconductor optical amplifiers (SOA) are frequently used. The coherence length dictating the depth range of imaging, Δz , is determined by the filtering scheme in the light source.

It is very common to have the light source be in the form of a ring cavity so that output power is maximized and amplified spontaneous emissions from the SOA are mostly rejected. While many laser sources are in development, two of the most commonly swept-sources are the fourier-domain-mode-locking (FDML) laser [14] and spinning polygon mirror-based laser [35]. A simple schematic of the FDML laser is shown in Figure 2-6. In this laser set-up, an SOA acts as the laser gain medium, a fiber Fabry-Perot filter (FFP-TF) acts as an optical bandpass filter for active wavelength selection, and km lengths of standard single mode fiber (SMF 28e) increases the cavity length so that the entire frequency sweep can be stored inside the cavity. To manage the dispersion in these long length fibers, fibers with different dispersion characteristics are combined to minimize dispersion such that different wavelengths within the spectral bandwidth experience the same round trip time. The FFP-TF is driven sinusoidally with a frequency proportional to the the optical roundtrip time of light in the cavity, or a harmonic thereof. The advantage of this laser is that it is not necessary to build up lasing from amplified spontaneous emission repeatedly, thus

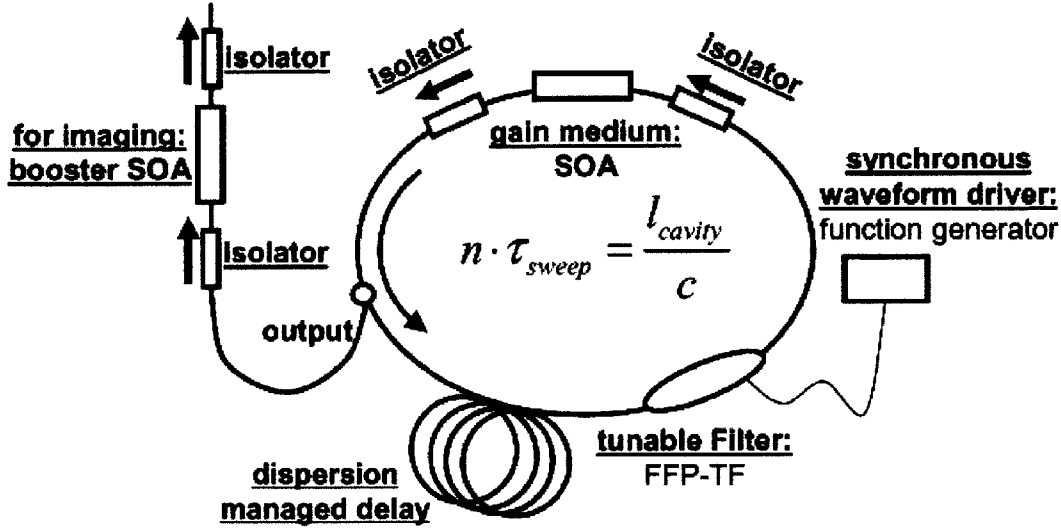


Figure 2-6: Schematic diagram for FDML laser; FFP-TF = tunable Fabry-Perot filter [14]

enabling for much higher tuning speeds than prior swept source designs. Gaussian spectral shapes with A-lines rates on the order of 1 MHz can be achieved with FDML lasers, although they are currently limited to ~ 7 mm depth ranges, partly due to limited bandwidths of digitizers. These and other tunable high speed lasers underscore the importance of having data-efficient OCT system.

Another typical design of a wavelength-swept source is shown in Figure 2-7 [35]. In this implementation of swept-source laser, light is amplified by an SOA and sent to a polygon scanning filter. The filter returns one wavelength at a time back to the fiber-ring laser cavity and 90% of this circulating light is output via a coupler. 10% of that light is directed toward a trigger circuit that provides the external trigger for the data acquisition board. A schematic of this polygon scanning filter is shown in Figure 2-8 [19]. This filter comprises of a diffraction grating that angularly disperses the light, a telescope of two lenses with focal lengths F_1 and F_2 , and a polygonal spinning mirror (typically 72 facets). A collimated Gaussian beam that comes from the cavity is incident upon the grating at an angle, α , and diffracts as a function of wavelength, λ , with an angle β . According to the grating equation, the filter's tuning

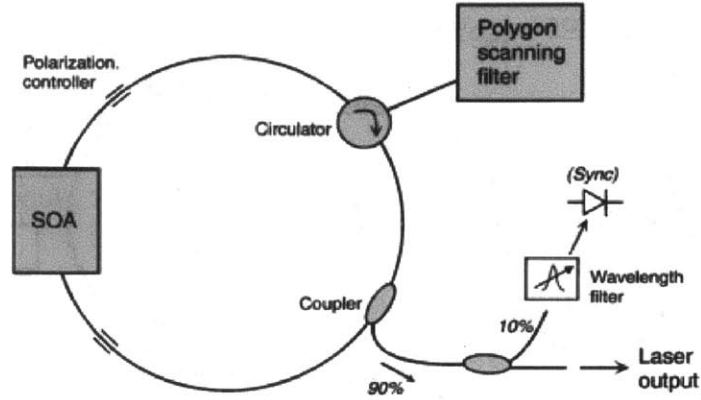


Figure 2-7: Swept source laser cavity with spinning polygon mirror filter [35]

range is [19, 20, 35],

$$\lambda = p(\sin \alpha + \sin \beta) \quad (2.29)$$

where p is the grating pitch as shown in Figure 2-8b. The center wavelength, λ_0 , of the spectral bandwidth is the wavelength for which β_0 is the angle between the optical axis of the telescope and the grating normal. The instantaneous linewidth of light from the filter output is given by [19],

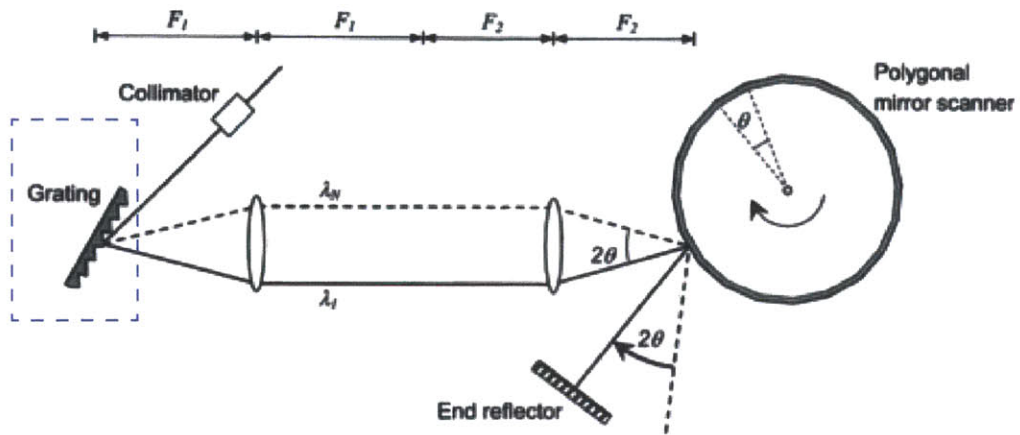
$$\delta\lambda_{FWHM} = \lambda_0 A(p/m) \cos \alpha / W \quad (2.30)$$

where $A = \sqrt{4 \ln 2} / \pi$, m is the diffraction order and W is the $1/e^2$ width of the Gaussian beam at the collimator. Given that the facet-to-facet polar angle of the polygon, $\theta = 2\pi/N \approx L/R$, where N is the number of facets, L is the facet width, and R is the radius of the polygon, then the free spectral range (FSR) is shown to be [19],

$$\Delta\lambda_{FSR} = p \cos \beta_0 \frac{F_2}{F_1} \theta \quad (2.31)$$

This denotes the spectral spacing of the two wavelengths that are retroreflected from different facets of the polygon, and ultimately this determines the spectral bandwidth, $\Delta\lambda$, of the laser source. In alignment of this laser, this spectral bandwidth is maximized so that good axial resolution can be achieved as per equation 2.28 [35].

(a)



(b)

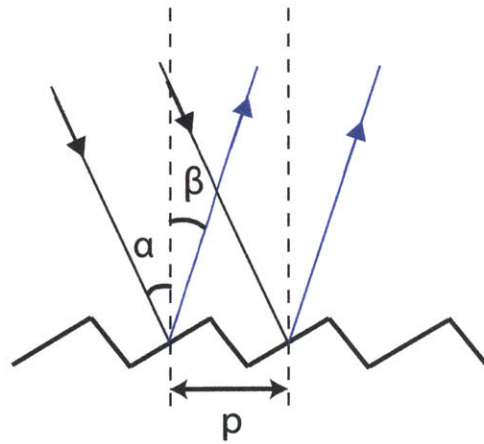


Figure 2-8: (a) polygon mirror based spectral filter [19] (b) schematic of diffraction grating where α = incident angle and β = diffraction angle

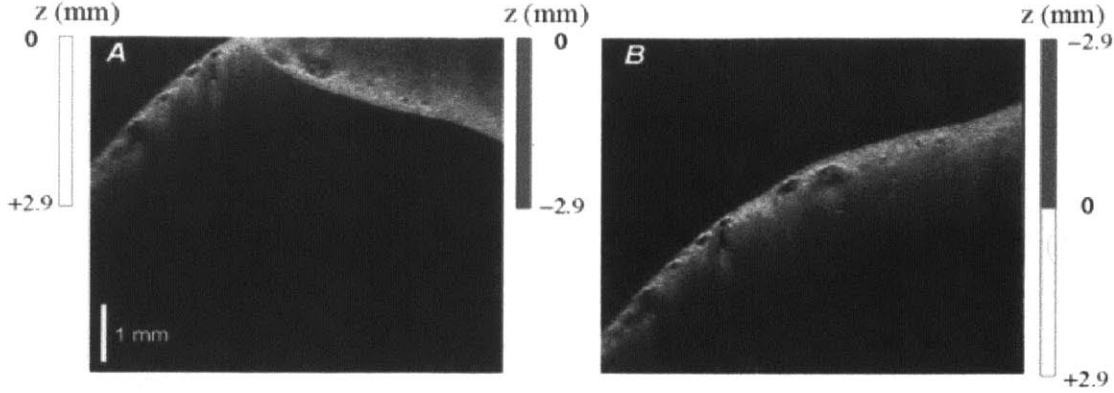


Figure 2-9: (A) Image segments that fall in both $+z$ and $-z$ regions overlap without complex conjugate removal (B) Image segments can be removed with conjugate demodulation [37]

For the purposes of demonstrating the optical subsampling concept, a polygon-based laser cavity was used because of its ease of construction and its stability over long times. However, optical subsampling can be incorporated into the FDML laser and other high-speed laser designs.

2.2.4 Complex-Conjugate Demodulation

Interference fringe signals that were measured with photodetectors are inherently real (Hermitian symmetric) signals and as such introduce complex-conjugate ambiguity. Recall that depth reflectivity information is encoded in the frequency of the cross-correlation term according to equation 2.15. Assuming that tuning is linear in k -space, then equation 2.14 represents the detector current and the frequency is given by $f_{sig} = |\frac{\alpha}{\pi}z|$. However, positive ($+z$) and negative ($-z$) cannot be distinguished after the Fourier transform, resulting in overlapping of signals from depths in front of and behind the matched optical path distance ($\Delta z = 0$). Initial FD-OCT interferometers required the sample to be placed on either the $+z$ or $-z$ region to avoid overlap such as in Figure 2-9A. However, this halves the usable depth range and makes imaging with such constraints difficult. For example with polygon based lasers, which typically have instantaneous linewidths $\delta\lambda \approx 0.1\text{nm}$, this half depth

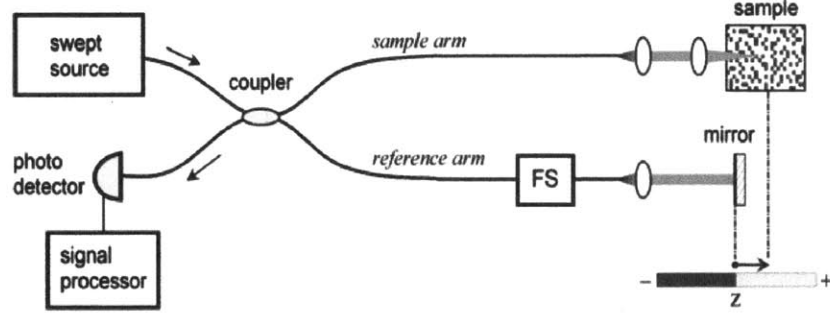


Figure 2-10: Schematic for a frequency shifter in the reference arm [37]

range would correspond to 4mm depth range.

Numerous techniques have been developed to remove the conjugate ambiguity and double the depth range. One commonly used technique is to add an acousto-optic frequency shifter (AOFS) in the reference arm of the interferometer as shown in Figure 2-10 [37]. This results in a shift of Δf in the frequency domain so that now the frequency of the fringe is given by [4,37],

$$f_{sig} = \left| \frac{\alpha}{\pi} z + \Delta f \right| \quad (2.32)$$

While the Fourier transform of the detector current i_{det} is still Hermitian symmetric, the shift of places signals from $+z$ depths to the right of Δf and $-z$ depths to the left of Δf as shown in Figure 2-11. This separates image segments from either side of the path matched delay and results in a continuous image with no overlap (Figure 2-9B).

This frequency shifter method was used to demodulate conjugate ambiguity in this work because of it's ease of integration and availability in the laboratory. However, it is evident that this technique forces a doubling in signal bandwidth since both the positive and negative delay signals are shifted to the frequency spectrum now contains frequencies from [37],

$$\Delta f - \frac{\alpha}{\pi} z \leq f_{sig} \leq \Delta f + \frac{\alpha}{\pi} z \quad (2.33)$$

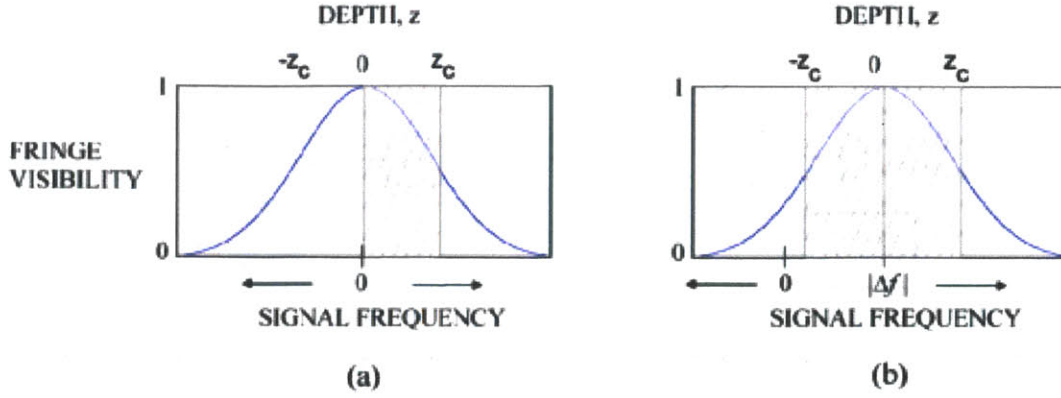


Figure 2-11: (a) without the frequency shifter, only the positive frequency region can be used (b) with the frequency shifter both positive and negative frequency regions can be used but entire spectrum is moved to Δf [37]

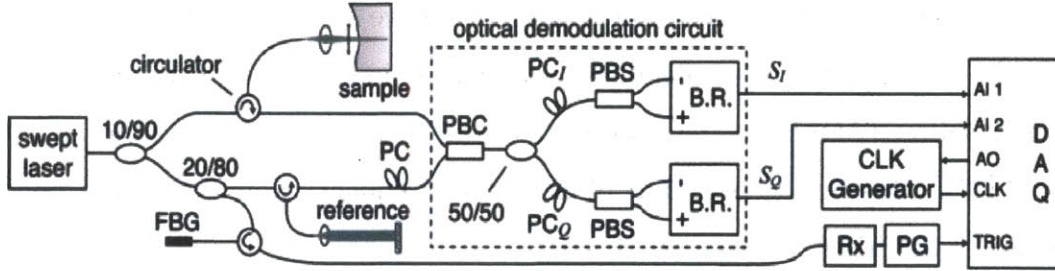


Figure 2-12: Diagram of swept-source FD-OCT system with polarization based conjugate demodulation (dashed box). In phase (S_I) and quadrature (S_Q) signals generated with the manipulation of polarization controllers PC_I and PC_Q . Each A-line is synchronized with a TTL signal generated by a fiber-bragg grating (FBG) [31]

Since the overall goal of optical subsampling is to minimize acquisition bandwidth, a demodulation scheme that does not require frequency doubling will be used in future works. An example of one such interferometer is shown in Figure 2-12 [31]. The optical demodulation circuit (dashed box) uses polarization-based biasing [38] to generate an in-phase ($S_I \propto A \sin \theta$) and a quadrature ($S_Q \propto A \cos \theta$) signal. Since this set-up utilizes two separate detection arms for quadrature detection, frequency shifting is not necessary and the system is more bandwidth efficient. It is important to note that in the context of optical subsampling, complex-conjugate removal is essential for prevention of image overlap, as discussed further in section 3.3.

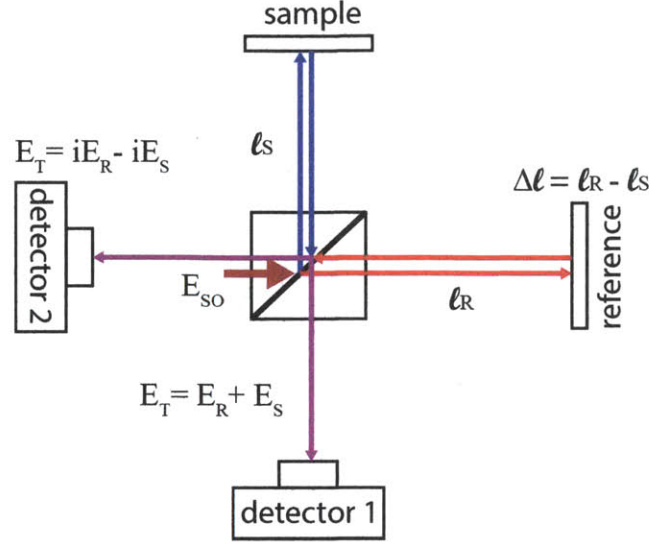


Figure 2-13: Schematic of balanced detection set-up wherein two detectors, D1 and D2, record interference fringes that are 180° out of phase. E_{SO} = input source light, E_R = electric field returning from reference arm, E_S = electric field returning from sample arm, E_{T1} = total electric field at D1, E_{T2} = total electric field at D2

2.2.5 Data Acquisition

Balanced Detection

Balanced detection takes advantage of the π phase shift between the two output ports of the beam splitter in the. Recall that in the Michelson interferometer (Figure 2-1), light is split into the sample and the reference arms and results in a cosinusoidal interference pattern at the detector. In this simplified derivation of irradiance in equation 2.4, amplitude of phase variations of the beam splitter and mirrors were not considered. It is apparent from the ABCD matrix of a 50/50 beamsplitter that there is amplitude and phase modulation of the light travelling through the beamsplitter [5]:

$$\begin{bmatrix} -\frac{1}{\sqrt{2}} & \frac{i}{\sqrt{2}} \\ \frac{i}{\sqrt{2}} & -\frac{1}{\sqrt{2}} \end{bmatrix} \quad (2.34)$$

Similarly, light reflecting from mirrors or samples result in 180° phase shifts. Figure 2-13 is a modified schematic of the Michelson interferometer with two separate

detection arms and input source light of E_{SO} . Assuming that,

$$E_R = r_R \frac{i}{\sqrt{2}} \frac{1}{\sqrt{2}} E_{SO} \quad (2.35)$$

and

$$E_S = r_S \frac{i}{\sqrt{2}} \frac{1}{\sqrt{2}} E_{SO} \quad (2.36)$$

where r_R is the reflectivity in the reference arm and r_S is the reflectivity in the sample arm, then the irradiance in detector 1 is:

$$I_1 = E_{T1} E_{T1}^* = (E_R + E_S)(E_R + E_S)^* = |E_R|^2 + |E_S|^2 + 2|E_R| |E_S| \cos(2k\Delta l) \quad (2.37)$$

whereas the irradiance in detector 2 is:

$$I_2 = E_{T2} E_{T2}^* = (iE_R - iE_S)(iE_R - iE_S)^* = |E_R|^2 + |E_S|^2 - 2|E_R| |E_S| \cos(2k\Delta l) \quad (2.38)$$

Notice sign change between the two irradiances. To achieve balanced detection, equation 2.38 is subtracted from equation 2.37. This detection scheme removes the DC component as well as reduces the source's random intensity noise (RIN), i.e. noise resulting from mode hopping and/or mode competition in the laser source. Furthermore, balanced detection can suppresses self-interference noise resulting from backreflections of components within the laser as well as improve fixed pattern noise by reducing strong background signal from the reference arm [18].

Nonlinear Sampling

As we discussed in equation 2.14, when the source tunes wavenumbers in a linear fashion (linear in k -space), depth (z) can be inferred from the frequency of the optical fringe via a simple Fourier transform. However, tuning is often not performed linearly in k -space, thereby resulting in an instantaneous frequency that is a function of time

instead of constant. For instance, if

$$k = k_0 + \frac{dk}{dt}t \quad (2.39)$$

the expression for instantaneous frequency becomes

$$f = \frac{1}{\pi} \frac{dk}{dt} z \quad (2.40)$$

Nonlinearity in the tuning curve of the laser results in chirping of the signal and degradation of axial resolution in the depth space (z -space). In the case of a polygon-mirror based swept source laser, described in section 2.2.3, the diffraction grating induces a linear- λ space tuning. To avoid degradation of axial resolution, the detector output may be sampled non-uniformly in time so as to produce uniform sampling in k -space. Alternatively, the detector output may be sampled uniformly in time while in the processing stage, the data is re-interpolated to be uniform in k -space. This latter method is commonly used in practice as noted in section 5.3. It should be highlighted that the frequency is proportional to the sweep speed of the laser, proving the salient concept that the faster the tuning rate of the laser (also termed A-line rate) the higher the frequencies of the OCT signals.

Chapter 3

Optical Subsampling in OCT

In the previous chapter, many principles of continuously swept OCT systems were reviewed; now concepts that are specific to subsampling will be introduced. This chapter begins with a review of relevant published works and then examines how optical subsampling is applied to OCT systems. The relationship between frequency comb filters and imaging parameters is discussed to clarify technical concepts required to understand imaging results in following chapters.

Some research content in the following sections was published in:

Meena Siddiqui, Benjamin J Vakoc. Optical-domain subsampling for data efficient depth ranging in Fourier-domain optical coherence tomography. *Optics Express*, 20(16):17938-17951, 2012

3.1 Relevant Work

As discussed in section 1.2, increasing the ranging depth and/or decreasing the sensitivity roll off of OCT imaging systems improves image quality as well as clinical versatility. Recall that the coherence length/ranging depth, Δz , of light is associated with the instantaneous linewidth, $\delta\lambda$, or instantaneous bandwidth, δf , of the light

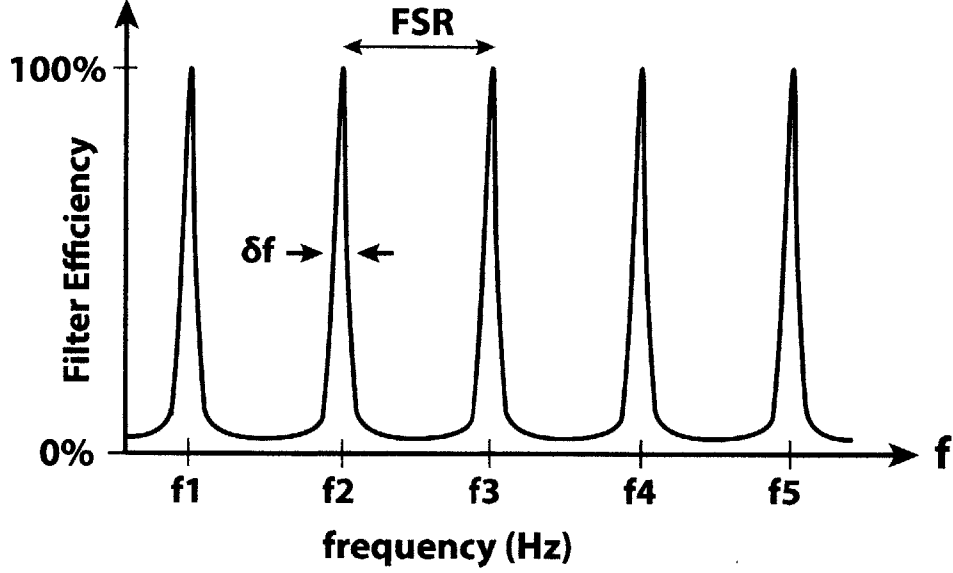


Figure 3-1: Sample Fabry-Perot (FP) transmission spectrum; δf = instantaneous frequency, FSR = free spectral range

source [4]:

$$\Delta z = \frac{\lambda_0^2}{4n\delta\lambda} = \frac{c}{4n\delta f} \quad (3.1)$$

where $c = 3 \times 10^8$ m/s, the speed of light in free space. In most modern OCT systems, inability to reduce this linewidth severely limits the ranging depth. For instance, FDML lasers discussed in section 2.2.3 suffer a -5 dB sensitivity drop over a 3mm depth range [13,15]. Similarly, polygon-based OCT lasers have ranging depths on the order of 5mm [34]. One method of reducing this instantaneous linewidth is to introduce a narrow passband spectral filter into the laser cavity. Various groups explored using a Fabry-Perot (FP) etalon as the filtering component in order to achieve better sensitivity in their principle imaging range [2,3,17,30]. FP etalons are frequency comb filters that pass a narrow and discrete sets of wavelengths while suppressing others. Figure 3-1 shows a sample schematic of a FP that transmits frequencies f_1, f_2, f_3, \dots with FWHM bandwidth, δf . The spectral distance between these highly transmitted wavelengths defines the free spectral range (FSR) of the etalon.

When swept sources were first employed in OCT, it was believed that they needed to

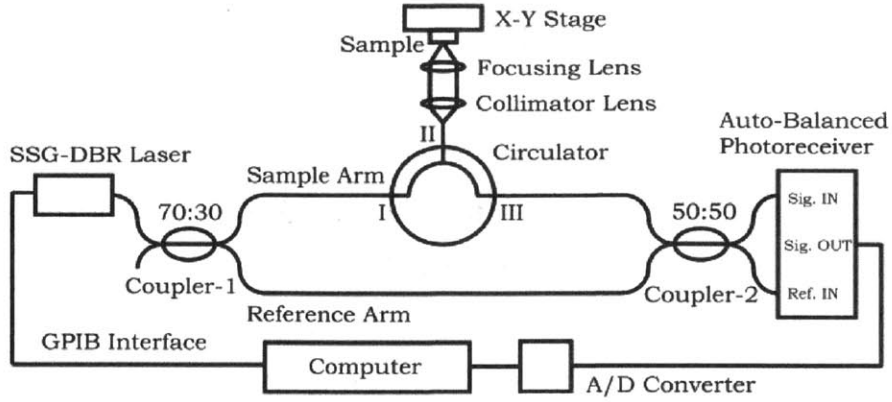


Figure 3-2: Superstructure-grating distributed Bragg reflector (SSG DBR) set-up for demonstrating discrete wavelength swept laser for OCT [2]

be continuously tunable, however, in 2005 Amano *et al.* provided a first demonstration that mode hopping in the laser source does not affect image data [2]. In their derivation, they showed that for a discretely swept laser with wavenumber $k_i = k_0 + i\delta k$ where $i = 1, 2, 3, \dots, N_S$, the detector current analogous to equation 2.14 is [2]:

$$i_{det}(t) = \frac{\eta q}{h\nu} (P_r + P_0 \int r^2(z) dz + 2\sqrt{P_r P_0} \int r(z) \Gamma(z) \cos(2k_i z + \phi(z)) dz) \quad (3.2)$$

and that abrupt changes in phase owing to mode hopping does not register in the interference cross correlation term, which can be written as [2],

$$i_{det}(t) = \frac{\eta q}{h\nu} 2\sqrt{P_r P_0} \cos(2k_i z_0) \quad (3.3)$$

Here the assumption is that a single reflector is placed in the sample arm at $z = z_0$ and that the coherence function $\Gamma(z) = 1$ because of the long coherence length of light in this filtered source. To experimentally demonstrate that discontinuously tuned lasers can be stably built for OCT imaging purposes, they designed a superstructure-grating distributed Bragg reflector (SSG DBR) based imaging system, as shown in Figure 3-2 [2]. Light emitted from the SSG DBR source was coupled into a single-mode fiber-optic Mach-Zehnder interferometer. This laser emitted light from 1533.17

nm to 1574.13 nm in approximately 0.1 nm steps (FSR equivalent to 0.1 nm) with $N_S = 400$ wavelength samples total.

The SSG DBR set-up affirmed discrete swept source lasers for use in OCT, however their experimental set-up was not suitable for imaging because of the low spectral bandwidth (40 nm) and very low scan speeds (250 Hz A-line rate). This work was followed up by Tsai *et al.* in 2009, who adapted a frequency comb swept laser into an FDML imaging system (Figure 3-3) [30]. This ring cavity is identical to that shown in Figure 2-6 with the addition of a frequency comb fiber FP filter, which had an instantaneous bandwidth $\delta f \approx 2.5$ GHz and an $FSR \approx 25$ GHz. This resulted in a discretely sampled OCT laser; however, the focus of the study was to reduce the sensitivity roll (from -5 dB to -1.2 dB) over their 3 mm principle imaging range rather than to increase the ranging depth and/or minimize the acquisition bandwidth of the imaging system. Interestingly, they reported that interferometric signals that have frequencies higher than $\frac{1}{2}$ of the optical sampling rate, $\frac{1}{2}N_S$, were aliased into their principle range of 3 mm. This same aliasing phenomenon was also reported by Jung *et al.* who constructed an external frequency comb filter for SD-OCT around the same time [17].

In this work, we take advantage of this aliasing phenomenon to drive down the number of samples N_S needed to image tissue over a wide ranging depth. We will provide the first demonstration that a swept frequency comb laser can be used to simultaneously increase ranging depth (from ~ 5 mm to ~ 10 cm) while minimizing acquisition bandwidth.

3.2 Sparsity in Extended Depth Range OCT

Penetration depth is limited by tissue opacity to 1-2 mm regardless of the imaging depth range, as discussed in Figure 1-6. Thus, in an extended depth-range OCT embodiment, a typical A-line will contain regions of negligible signal both superficial

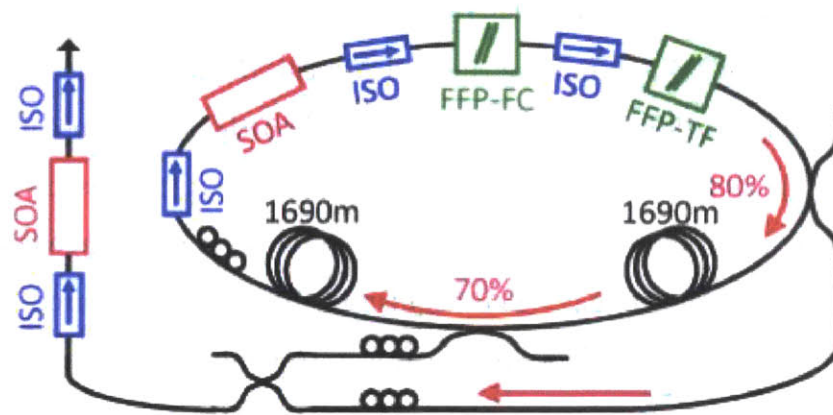


Figure 3-3: A frequency-comb FDML laser. FFP-FC = frequency comb fiber Fabry-Perot filter; FFP-TF = tunable Fabry-Perot filter; ISO = isolator; SOA = semiconductor optical amplifier [30]

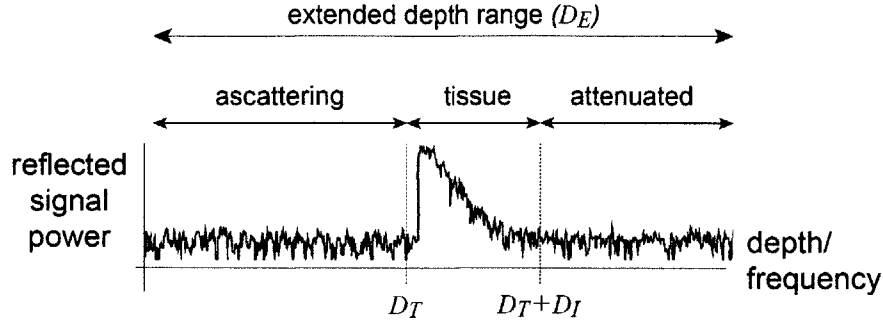


Figure 3-4: OCT signal in an extended depth range

to the tissue surface, and at delays associated with locations deeper than 1-2 mm beyond the tissue surface. Between these signal-absent regions will be the tissue signal region (Figure 3-4). Acquiring this full A-line is data inefficient because a large fraction of the acquisition bandwidth is dedicated to the signal-absent (ascattering or attenuated) regions. However, because the location of the tissue signal is not known *a priori*, a limited and targeted acquisition of the depth range containing the tissue is practically challenging. The acquisition bandwidth required for extended range imaging can be reduced by finding a way to eliminate this inefficiency while preserving the ability to image over extended depth ranges.

3.3 Bandpass Sampling

Approaches for sampling bandwidth limited signals have been studied extensively in communications and information theory [1, 8, 33]. Consider a bandwidth limited signal located at f_C with a bandwidth B (Figure 3-5a,b). Nyquist sampling at $2f_U$ captures this signal fully, but is data inefficient because a large fraction of the detected bandwidth does not contain signal (Figure 3-5b). Alternatively, because the signal is bandwidth limited, sampling the signal directly at twice its bandwidth, i.e., $2B$, can capture its information content (Figure 3-5c). This approach is termed subsampling because it samples the signal at rates below twice the highest frequency content of the signal, $2f_U$. Higher frequencies appear in the baseband window through aliasing (Figure 3-5d,e).

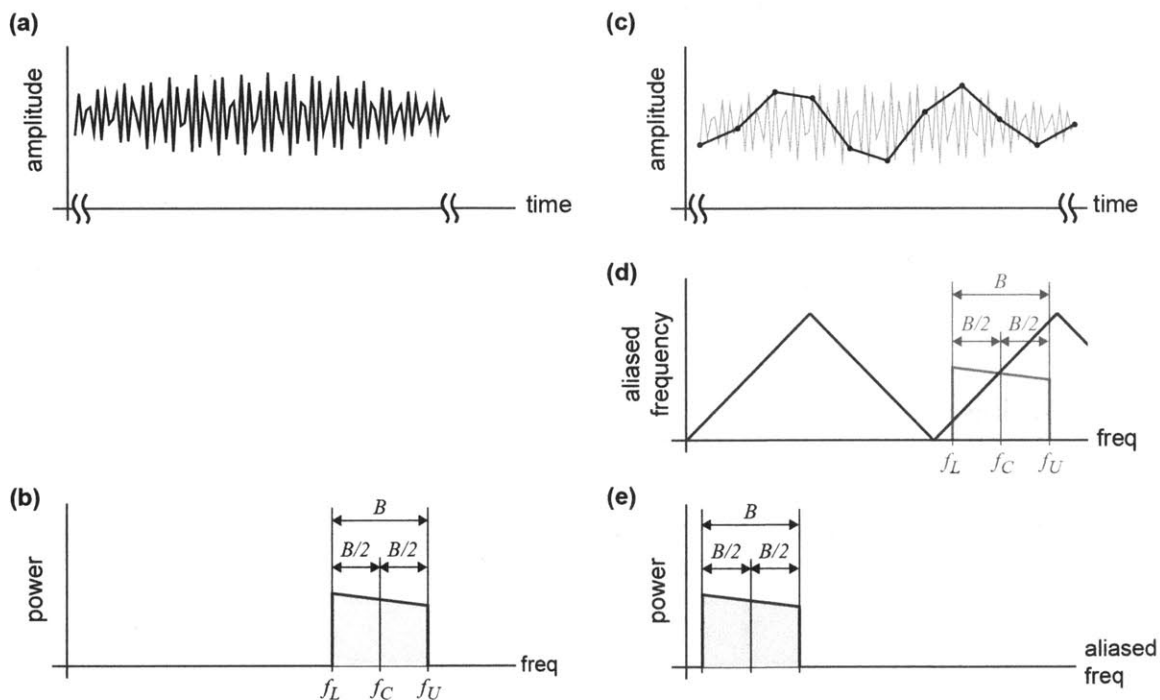


Figure 3-5: Subsampling of bandwidth limited signals. (a,b) A bandwidth limited signal sampled at twice its highest frequency content ($2f_U$) yields the full frequency content. However this is data inefficient because non-aliased sampling frequencies increase with signal frequency. (c-e) Direct subsampling of the signal at twice its bandwidth ($2B$) captures its information content by repeated aliasing of the original frequency space to the baseband window.

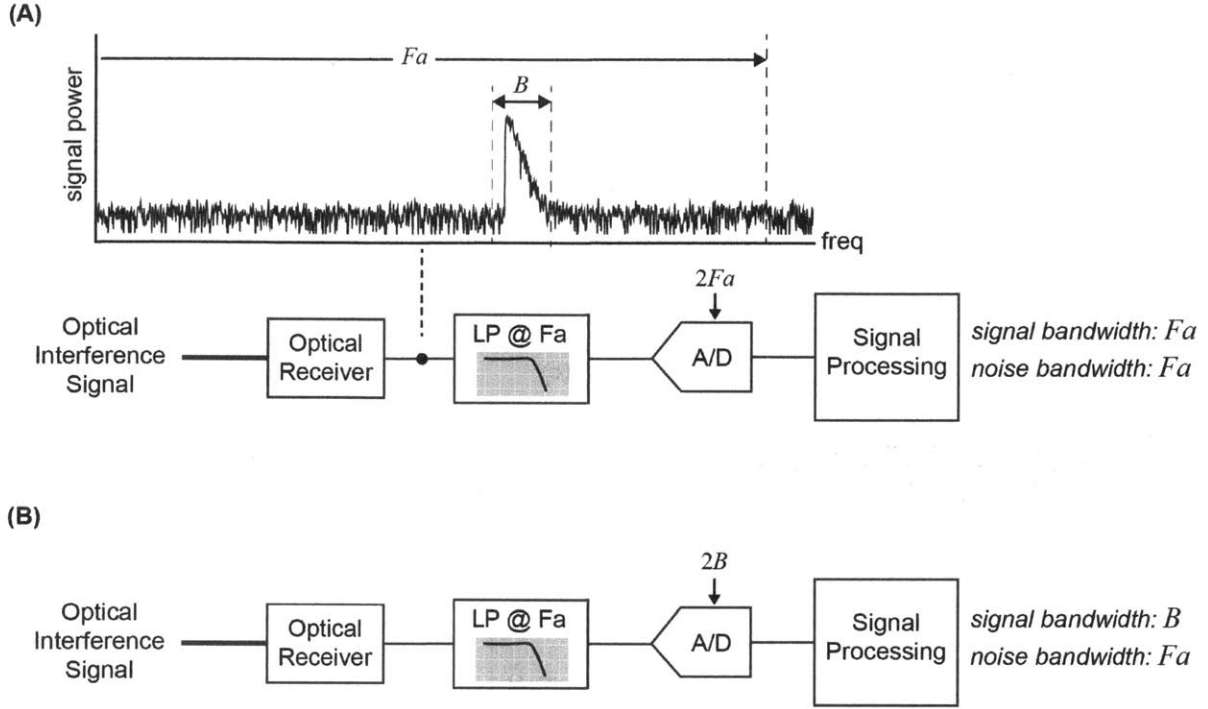


Figure 3-6: Electrical-domain subsampled receiver designs. An electrical-domain subsampling receiver (B) must retain the full RF bandwidth of the conventional fully sampled receiver (A), but it utilizes a lower digitization clock rate ($2B$ vs. $2F_a$). The resulting digital acquisition bandwidth is reduced by the factor of (F_a/B) and the noise is increased by the same factor (assuming white noise).

3.3.1 Electrical-Domain Subsampling

The most straightforward implementation of subsampling is in electrical-domain, i.e., to maintain full RF bandwidth on all receivers but operate the digitization clock at a reduced rate. A conventional OCT receiver is shown in Fig 3-6A and the electrical-domain subsampling receiver is illustrated in Fig 3-6B. Here, the full interference fringe bandwidth is detected and transmitted to the digitizer, but is sampled at a rate of $2B$ rather than the Nyquist rate ($2F_a$) by the digitizer. By operating at a lower digitization rate, subsampling in the electrical-domain reduces the digital acquisition bandwidth required to capture the signal. However, by requiring full analog bandwidth, it also increases the noise proportionally by integrating noise across this large bandwidth into the aliased baseband window. For some applications requiring a modest decrease in acquisition bandwidth, the associated noise increase might be an

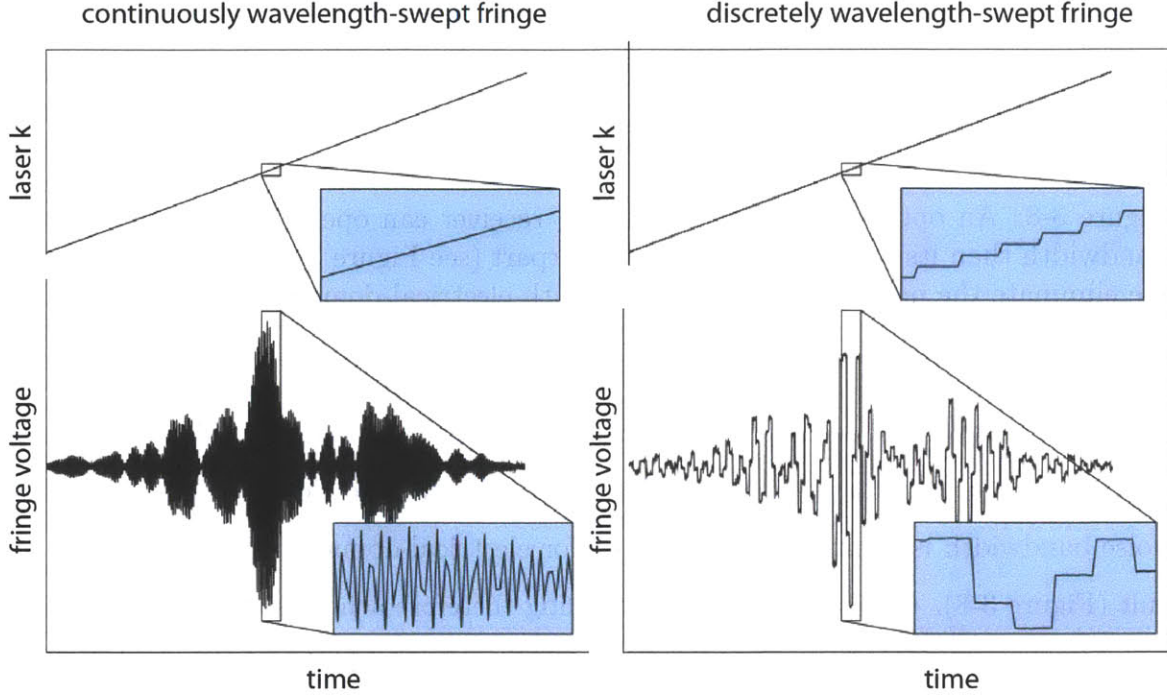


Figure 3-7: An illustration of wavelength evolution and fringe signals generated from a continuously wavelength swept laser (left) and an optical-domain subsampled laser source (right).

acceptable penalty to achieve a corresponding reduction in digital acquisition bandwidth. For more aggressive applications of subsampling, this noise penalty would be prohibitive. In this work, we describe a strategy that implements subsampling in the optical-domain such that acquisition bandwidth reductions can be achieved *without* proportional penalties in noise.

3.3.2 Optical-Domain Subsampling

In addition to the electrical-domain, subsampling can be implemented in the optical-domain by limiting the wavelengths used to probe the sample, i.e., by probing the tissue with a set of discrete wavelengths rather than a continuously wavelength-swept source. Theoretical fringe signals of a continuously swept-wavelength and wavelength-stepped (subsampling) source are illustrated in Figure 3-7. By stepping between wavelengths, multiple depth locations are aliased optically to the same fringe frequency,

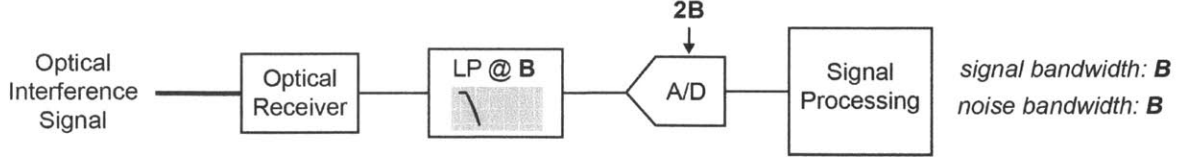


Figure 3-8: An optical-domain subsampling receiver can operate with lower analog bandwidth than its electrical-domain counterpart (see Figure 3-6), and can in principle eliminate the noise penalty associated with electrical-domain subsampling.

achieving an optical baseband compression of a large depth range. This fringe can be captured using reduced analog and reduced digital bandwidth receivers, and the noise bandwidth is less than that required for electrical-domain subsampling as a result (Figure 3-8). Optical-domain subsampling therefore achieves the compression of subsampling without a proportional noise increase. Some of the central properties of optical-domain subsampling is described next.

Acquisition bandwidth

Recall from equation 2.26 that in continuous FD-OCT, the number of optical wavelengths samples per axial scan was the ratio of spectral bandwidth and instantaneous linewidth. Thus increasing the coherence length i.e. 20-fold increases the acquisition bandwidth 20-fold. However, this is assuming that you optically sample at intervals equal to the instantaneous linewidth. With a frequency comb source, the sampling interval is the FSR of the filter and the number of samples within the spectral profile, N_S , is now given by,

$$N_S = \frac{\Delta\lambda}{FSR} \quad (3.4)$$

This idea is better demonstrated in Figure 3-9 where a sample spectrum of the frequency comb filtered broadband light is drawn with an overlay of the laser's gain profile. This leads to the following equation for acquisition bandwidth,

$$BW = \frac{\Delta\lambda}{FSR} f_A \quad (3.5)$$

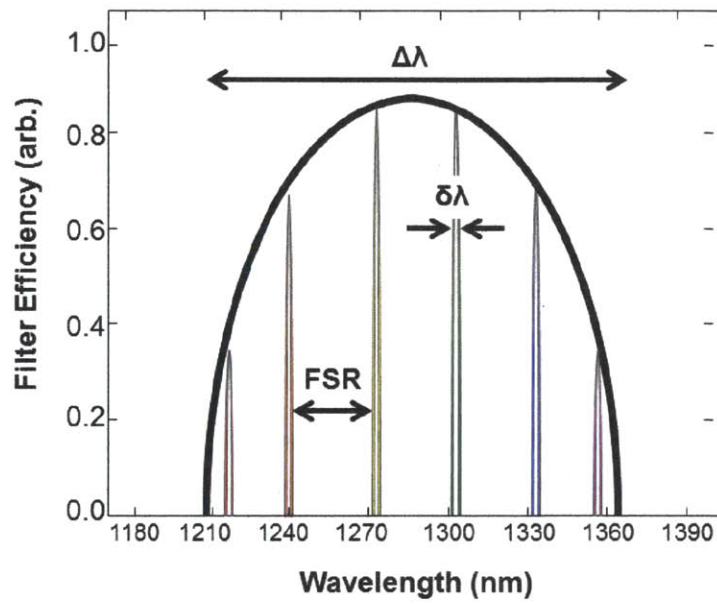


Figure 3-9: The ratio of the spectral bandwidth ($\Delta\lambda$) and free spectral range (FSR) determine the number of optical samples (N_S) in the laser. The instantaneous linewidth ($\delta\lambda$) can be decreased without affecting N_S in the subsampled laser

where again f_A is the A-line rate. Compare this to the bandwidth of the continuously swept source 2.27. Now the instantaneous linewidth has been decoupled from the equation for acquisition bandwidth and coherence length (and thereby imaging range) can be increased without necessarily increasing the acquisition bandwidth. In this work, we take advantage of this fact to significantly increase the ranging depth without increasing the acquisition bandwidth of OCT signals. Because of the sparsity described in section 3.2, no information is lost. Instead, the effective imaging depth (also referred to as the baseband window depth), which contributes to data bandwidth, can be smaller than the ranging depth, Δz . The baseband window depth must be at least the size of the penetration depth of light into the tissue of interest (as shown previously in Figure 1-6) in order to avoid image overlap. Ideally, the window will be the same size as the penetration depth so that data bandwidth is not wasted.

Relationship between subsampled laser parameters and imaging parameters

The FSR in a subsampled source describes the size of the baseband aliased window, i.e., the depth extent of the baseband image. If we assume a constant spacing (in optical frequency) between wavelengths, and that complex demodulation is fulfilled, the FSR is related to the baseband window depth, L , by the following equation:

$$L = \frac{c}{2nFSR} \quad (3.6)$$

where c is the speed of light and n is the index of refraction of the sample medium. It makes sense intuitively that the baseband window and the FSR are inversely related because as can be seen in Figure 3-9, the larger the FSR the fewer wavelength samples that can exist within the laser profile. Assuming a fixed axial resolution then, the baseband window would have to be smaller to reflect the fewer optical samples that were used to probe the tissue. It is important to ensure that the baseband window depth L is greater than the depth extent of the signal (D_I in Figure 3-4) to eliminate signal overlap.

As in continuous swept-wavelength sources (equation 2.28), the source bandwidth $\Delta\lambda$ describes the axial resolution of the subsampled laser:

$$\delta z = \frac{2 \ln 2}{n\pi} \frac{\lambda_0^2}{\Delta\lambda} \quad (3.7)$$

As long as the index of the material n is not wavelength dependent, then the axial resolution should be the same throughout the A-line. Similarly, the ranging depth is inversely related to the instantaneous linewidth as described in the continuous FD-OCT lasers and in equation 3.1.

In the next chapter, a preliminary optically subsampled OCT system was constructed to allow these key principles of depth-compressive imaging to be experimentally demonstrated.

Chapter 4

System Design and Construction

In section 3.1 it was shown that Fabry-Perot (FP) etalons can significantly reduce instantaneous linewidth to increase the coherence length and sensitivity of OCT over very long ranges. We also saw that FP etalons also induce frequency-comb spectrum and result in discrete swept wavelength lasers [30]. We now use the FP in conjunction with a continuously swept laser to build the first optically subsampled source for use in OCT. The criterion for the optically subsampled laser was to have a simple implementation of optical subsampling for proof-of-concept experiments.

4.1 Optically Subsampled Laser

To generate the optical-domain wavelength stepped laser source, a continuously wavelength-swept laser based on a free space polygon mirror sliding filter was modified (Figure 4-1). A free space fused silica Fabry-Perot (FP) etalon (LightMachinery) was inserted into the laser cavity to select discrete and linear-in- k wavelengths. From section 3.3.2 we saw that the FSR of the FP is related to the principle imaging depth (a.k.a baseband window depth), thus we elected a FP with an FSR of 80 GHz (0.45 nm), providing a baseband window depth of 1.4 mm (assuming a tissue index of $n = 1.38$). The FP finesse, which is defined according to:

$$finesse = \frac{FSR}{\delta f} \quad (4.1)$$

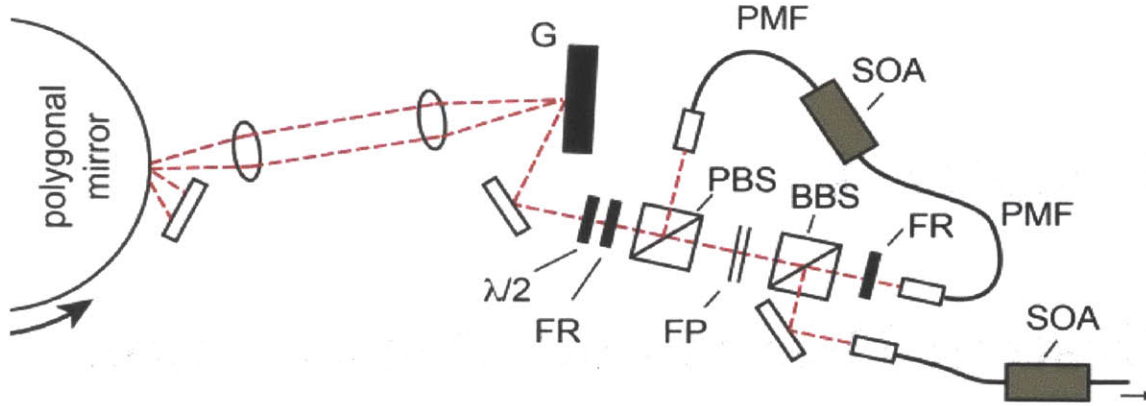


Figure 4-1: Sample figure of a free space wavelength swept laser with a Fabry-Perot (FP) etalon inserted in the cavity. PMF = polarization maintaining fiber; FR = Faraday rotator; BBS = broadband beam splitter; FP = Fabry-Perot; G = grating; PBS = polarization beam splitter; $\lambda/2$ = half wave plate

was specified as greater than 80 over a 100 nm spectral bandwidth and centered at 1300 nm. Recall that δf was the instantaneous bandwidth of the comb filter as indicated in Figure 3-1. The laser was implemented using a free-space optical circulator design, which allowed smaller cavity lengths and shorter build-up times for the laser than fiber-based cavities. The linewidth of the polygon-mirror based filter was designed to be approximately 0.21 nm (or $\delta f \approx 37$ GHz), providing sufficient extinction of the neighboring FP modes while retaining a high laser duty cycle. A booster amplifier was placed outside the laser cavity to compensate for power losses induced by the insertion of the FP filter. Output power was measured at ~ 46 mW. The laser was operated at 27 kHz for imaging experiments and 5.4 kHz for mirror translation experiments as presented in later sections.

It is clear from Figure 4-2 that the laser operates at frequencies/wavelengths given by the product of the transmission of two filters, the polygon filter and the FP etalon:

$$f = f_{\text{polygon}} \times f_{\text{FP}} \quad (4.2)$$

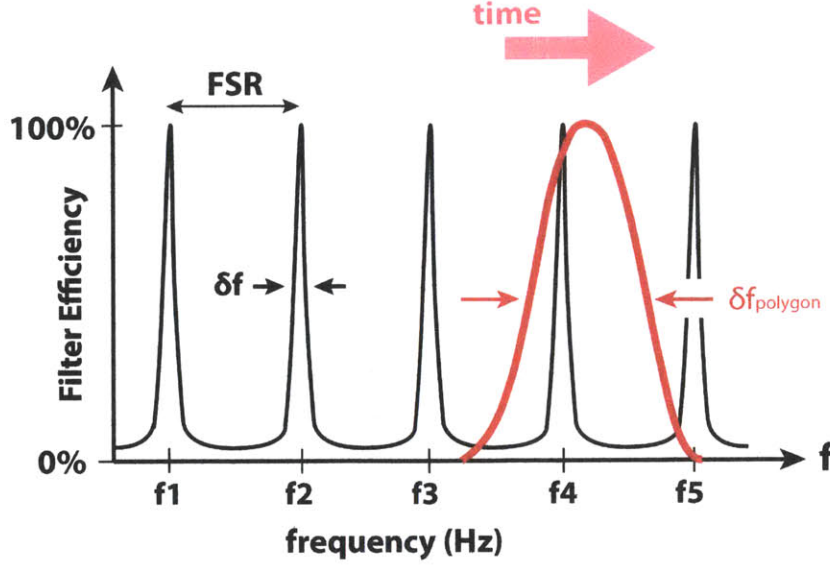


Figure 4-2: The instantaneous linewidth δf of the scanning polygon filter should be on the size scale of the FSR of the FP filter to allow smooth transition between wavelengths

The transmission function of the polygon filter reflects the continuous reflection of dispersed light from the grating and its spectral bandwidth was given in equation 2.31. The transmission of the FP filter is discontinuous as displayed in Figure 3-1 and is defined by the function [30]:

$$T(k) = \frac{(1 - R)^2}{1 - 2R \cos(2kL) + R^2} \quad (4.3)$$

where T is the transmission efficiency, R is the reflection coefficient, L is the cavity length in the FP resonator, and k is the wavenumber of the incident light. If the instantaneous linewidth of the polygon filter, $\delta\lambda_{polygon}$ is smaller than the FSR of the FP, then ideally one wavelength would exist in the cavity at a time. Practically, how-

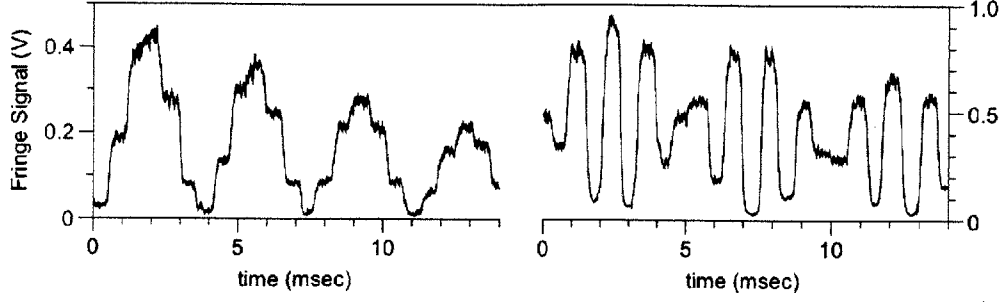


Figure 4-3: Interference fringe signals at two depths demonstrate optical-domain generation of baseband signals. Left: lower frequency fringe corresponding to a smaller optical path difference Δl ; Right: higher frequency fringe corresponding to a larger Δl

ever, the transition between the wavelengths are not smooth and there is modulation in the intensity of the laser output. We did indeed observe such intensity modulation from the output of this laser as further discussed in section 5.2.2.

4.1.1 Laser Parameters

Fringes

To examine the interference fringes, a separate Michelson interferometer was constructed. The A-line rate was reduced to 5.4 kHz, and the interferometer output was detected using a 200 MHz receiver (Thorlabs, BDB460C) without balanced detection. By operating at a lower A-line rate and using higher speed receivers, the higher frequency components and stepped nature of the fringe can be appreciated (Figure 4-3). This closely matched what was expected theoretically in Figure 3-7. As the reference arm was translated, the fringe properties repeated periodically, providing a first confirmation that subsampling was being performed in the optical domain.

Laser coherence length

To measure the laser coherence length, we used the imaging interferometer described in section 4.2.2. Fringe data were recorded from a fixed sample arm mirror while translating the reference arm over a 12.5 cm range (25 cm optical path variation).

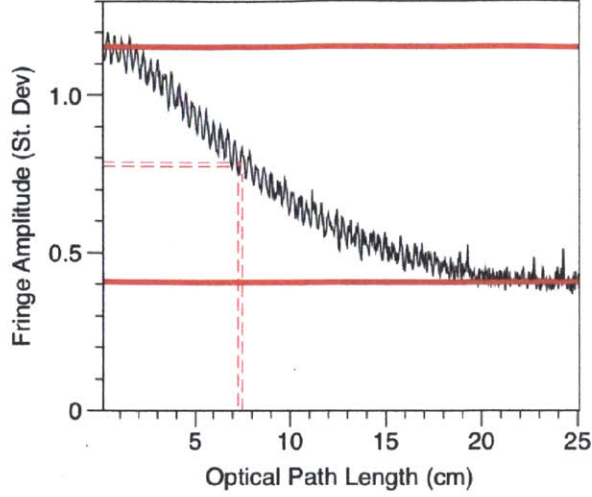


Figure 4-4: The measured coherence length of the optical-domain subsampled laser incorporating an intra-cavity FP etalon exceeded 7 cm.

Fringe visibility calculated as the standard deviation of the fringe showed a single-pass coherence length of approximately 7.4 cm (Figure 4-4). We noted that without the intra-cavity FP filter, the laser coherence length was limited to several millimeters, demonstrating that inclusion of the fixed FP etalon can both force optical-domain subsampling and also contribute to significant extension of the laser coherence length.

4.2 Data Acquisition

4.2.1 Preventing signal overlap in subsampled FD-OCT

To be effective in the context of imaging, subsampling must ensure that signals from each depth, within the penetration depth of tissue, can be measured independently from those at other depths, i.e., overlap artifacts must not compromise the resulting image. This requirement can be met straightforwardly when subsampling is applied to complex fringes, but is more challenging when applied to real fringes. To illustrate this, we generated a numerical OCT phantom structure, derived associated fringe signals from this phantom, and explored the effect of subsampling on the imaging

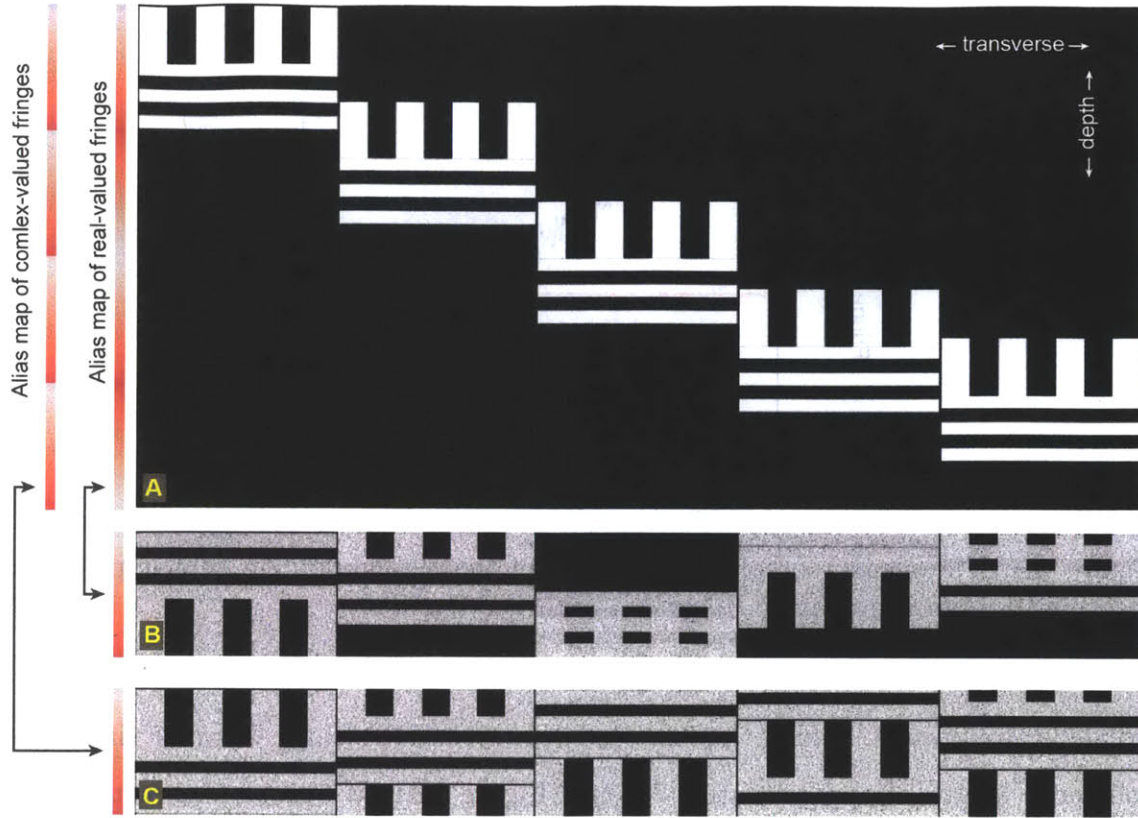


Figure 4-5: Real-valued and complex-valued signals are mapped differently into the aliased frequency space. For real-valued signals, signals located at varying locations (A) can induce distortions due to non-circular wrapping in the aliased image (B). For complex signals, wrapping is circular and overlap is avoided as long as the baseband window is large enough to contain the depth extent of the signal (C).

(Figure 4-5). First, we placed the phantom at varying locations in depth (Figure 4-5A). Next, we derived the associated fringes assuming continuous wavelength sampling across this depth range. We then subsampled the real-valued fringe data by a ratio of 1:4, and presented the compressed image (Figure 4-5B, showing only the positive frequencies). Note that the non-circular mapping of signal frequency to aliased frequency results in image overlap for most locations of the image. We then repeated this analysis but subsampled the complex fringe signal at a ratio of 1:8 (to give the same baseband window depth, the ratio was decreased by a factor of two because the signals are complex valued). In Figure 4-5C, the complex subsampled images are presented. Note that the image is wrapped circularly, and signals never overlap onto

itself for any depth location.

To achieve artifact-free imaging for arbitrary sample locations, it is necessary therefore to operate on complex OCT fringe data. Many approaches exist for extracting the complex optical interference signals in OCT, and a few were summarized in section 2.2.4. These have been used previously to separate signals from positive and negative delays and double imaging depth, but in the subsampled case, it directly prevents image overlap. It should be reiterated that dual detector techniques such as polarization-based demodulation have an acquisition bandwidth advantage over single detector techniques such as modulation with an acousto-optic frequency shifter (AOFS).

4.2.2 Interferometer

The interferometer used for data collection in following experiments is summarized in Figure 4-6. An AOFS at $\Delta f = 25$ MHz was used in the reference arm to provide complex fringe demodulation as discussed in section 2.2.4. Trigger signals were generated from a fiber Bragg grating (FBG) with a center wavelength chosen with sufficient overlap to one of the FP transmission peaks. The FBG bandwidth of 42 GHz was sufficiently small relative to the FPs FSR to ensure consistent trigger pulse generation from a specific FP transmission peak. Fringes were detected using balanced 80 MHz balanced receivers (New Focus, 1817-FC). The theory of balanced detection was discussed in section 2.2.5. The design in this interferometer was modified slightly to include two output channels, one for x -polarized light and one for y -polarized light. In this dual balanced interferometer, a beam splitter splits the light 50/50 into two different ports. Each port enters a polarization beam splitter, which further splits light into an x -polarized arm and a y -polarized arm. Both x -polarized arms are then received by a balanced receiver (BR1); the y -polarized arms are received in BR2. This dual detection scheme ensures that both x -polarized light and y -polarized light coming from the sample can be interfered and received. As discussed later in the

processing, the two channels can then be averaged to further reduce random noise and increase contrast in the image. Electronic low-pass filtering at 50 MHz was implemented prior to digitization at 100 MS/sec to prevent electronic aliasing.

4.3 Microscope

The design of focusing optics of the microscope is not affected by the subsampled source and as such have the same qualities as in conventional OCT systems as described in section 2.1.2. In this work, however, we used a modified microscope wherein a long focal length lens ($f = 10$ cm) was placed before the 2-axis galvometer mirrors instead of behind it (Figure 4-7). The loose focusing of the optical beam increased the depth-of-focus so that imaging could be performed over an extended depth range at a reduced transverse resolution of $\sim 96 \mu\text{m}$. The system also allows for an increased field-of-view (FOV) with dependence on how far away the sample was placed from the galvometer mirrors. This kind of imaging scheme is common in other *in vivo* imaging modalities such as white-light endoscopy, and can be very advantageous for screening applications where large volumes of tissue need to be scanned. Microscopy like this has not been possible in OCT before because imaging ranges have not been long enough to allow it. With the increased coherence length of our subsampled laser, we experiment with this alternative microscope and show that it is possible to image larger volumes.

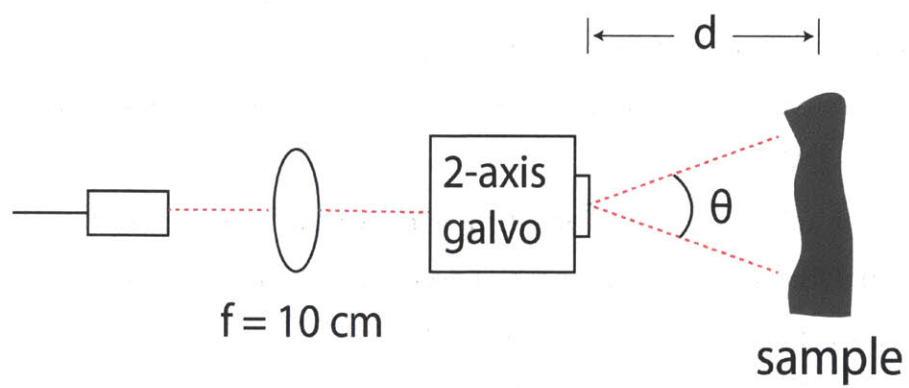


Figure 4-7: Microscope used in the subsampled OCT system. Focal length of lens = 10 cm; $\theta = 30^\circ$ FOV; d = distance between galvo and sample

Chapter 5

Performance and Imaging

The goal of this chapter is to discuss how processing of images were carried out and present evidence that the subsampled system actually enables imaging over long ranges with low acquisition data bandwidths. The results of a mirror translation experiment and tissue/object imaging experiment confirm compression of OCT signals over a long depth range into a baseband window of 6 MHz bandwidth (~ 1.4 mm baseband depth).

5.1 Mirror Translation Experiment

To examine the data compression provided by optical-domain subsampling, point spread functions (PSF) were acquired over a 15 mm (single-pass) optical path difference (Δz). The interference fringes between a sample mirror and reference mirror were recorded continuously as the reference mirror was translated with a motorized stage over 7.5 mm (double pass) at a constant speed. Hence, each A-line was measured at successively larger Δz values. Recall from equation 2.13 that the frequency of the fringe signal increases as Δz increases, thus a linear increase in frequency with depth was expected. Illustrated in Figure 5-1 is the detection receiver along with the frequency content of the A-lines over a subset of this 7.5 mm translation. This data was Fourier transformed in MATLAB and displayed as frequency vs. depth using the *imagesc* function; thus areas of the high intensity areas (white) correspond to

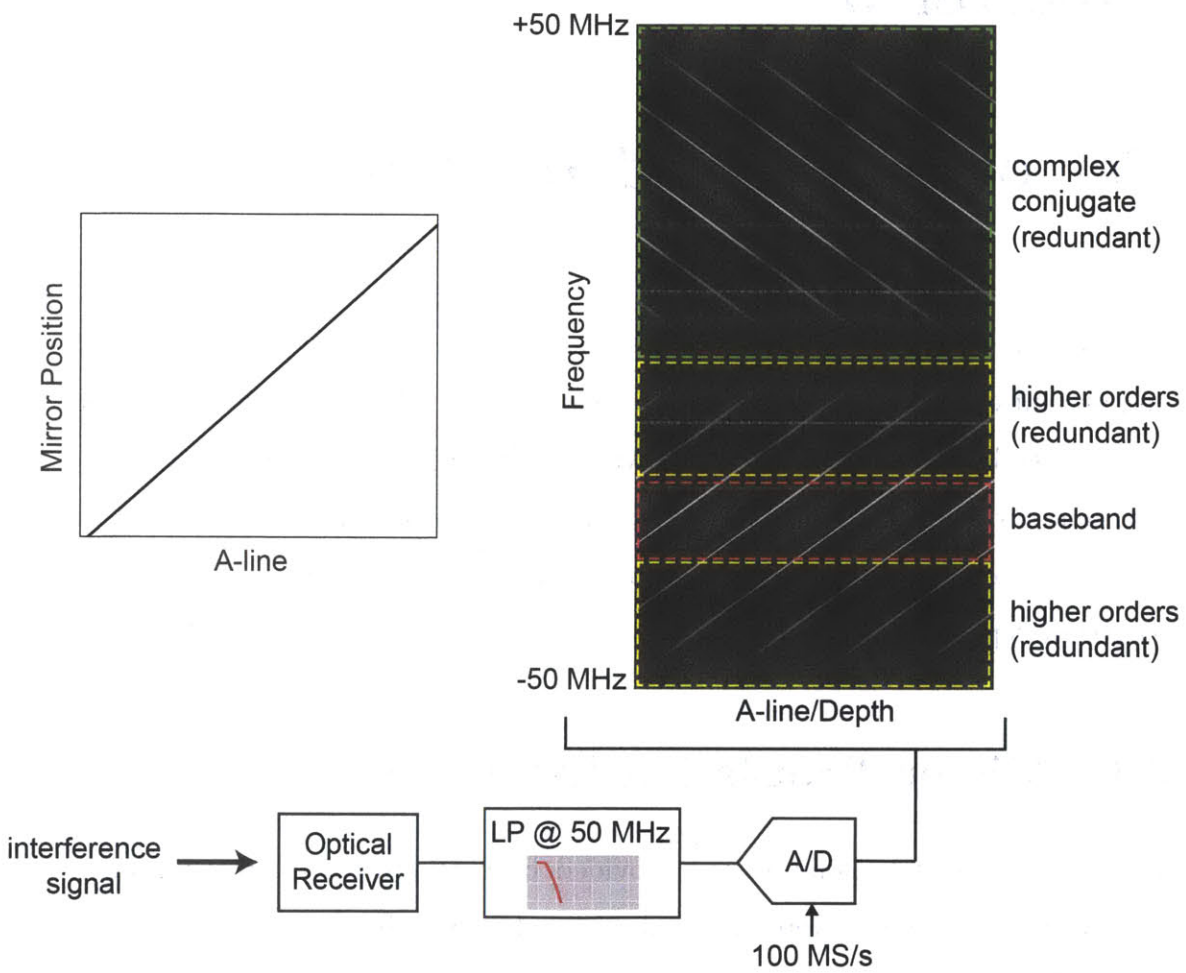


Figure 5-1: Experimental demonstration of optical-domain subsampled OCT. Interference fringes were acquired of a fixed sample while translating the reference arm mirror. The frequency content of the interference fringes demonstrates the wrapping of the mirror signal in the baseband window and presence of higher order powers.

the PSF and the black background indicates no/low signal. The image is divided into three regions; the baseband window region, the higher order harmonics, and the complex conjugate signals. Because of the 25 MHz AOFS, the fundamental frequencies (baseband window) was located in the center of the dataset. Recall from section 4.2 that the AOFS was used to provide complex signals and induce circular wrapping. The circular nature of wrapping is confirmed in the baseband window; when the fringe signal reaches the edge of the window, it circularly wraps back to the beginning (opposite side) of the window at the next incremental depth. This pattern continues over the extent of the 7.5 mm translation range, and confirms that even as depth increases the frequency of the signal does not exceed the baseband window bandwidth (approximately 6 MHz). Thus signals over an extended depth range are confined to a 6 MHz acquisition bandwidth. As shown in Figure 4-3, the fringe signals were discretized, thus there were higher order harmonics in the PSF signal, which became apparent because a 100 MS/s digitizer card was used. This was artifact that could easily be removed in future experiments with proper filtering. The signals were also repeated in the complex conjugate domain due to Hermitian symmetry of the real signals detected with the optical receiver.

5.2 Noise Analysis

5.2.1 Signal loss due to higher order harmonics

The stepped optical fringe generated by optical-domain subsampling contain some power in higher-order harmonics. The information content of these harmonics is redundant to the baseband window as shown in the previous experiment. However, the power lost to these higher-order harmonics reduces the signal power in the baseband window and affects the measurement SNR. To explore this further, we analyzed the frequency content of a simulated step-wise interference fringe as a function of location (Figure 5-2). These results demonstrate that there is a depth-dependent generation of higher-order harmonics. The depth-dependence can be explained by

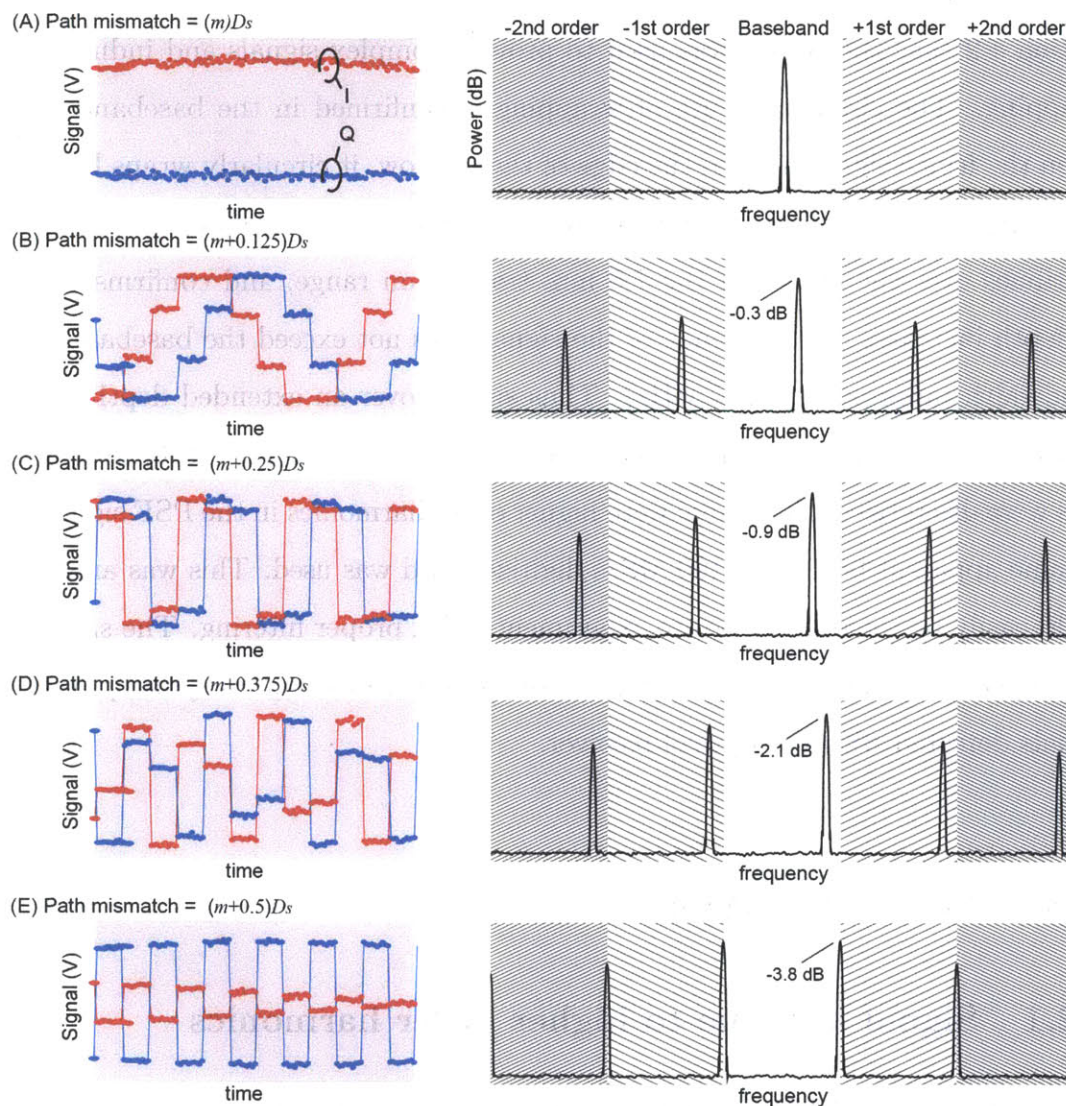


Figure 5-2: Optical-domain subsampling induces a small periodic loss in baseband signal strength due to its stepwise nature and the resulting placement of signal power into higher orders. The signal variation is limited to 3.8 dB over the aliased baseband depth window. m is an integer and D_s is the baseband window depth.

the varying magnitude of the step changes in associated interference fringes; greater magnitude of step changes occur at fringes that are closer to being critically sampled by the discrete set of wavelengths (Figure 5-2e). This corresponds to signals located at $(m + 0.5) * D_S$ where D_S is the baseband window depth and m is an integer; hence there is a maximum loss of ~ 3.8 dB in baseband signal power here due to higher-order harmonics.

5.2.2 High frequency intensity modulation of laser

As briefly discussed in section 4.1, a discretely stepped laser can lead to intensity modulations in the output if the transition between wavelengths is not smooth. This could happen in the case where the instantaneous BW ($\delta f_{polygon}$) is much smaller than the FSR of the FP filter so that the power in the laser drops significantly when the polygon filter is in between two FP transmission peaks (refer to Figure 4-2). However, it could also occur in the case where the instantaneous BW is much larger than the FP FSR so that multiple modes are competing in the laser and causing instability. To investigate whether our subsampled laser was experiencing such intensity modulation, a shutter blocked the sample arm in the interferometer (Figure 4-6), and the background signal was measured. Background signal is typically measured to remove noise coming from components within the interferogram and laser that are not derive from the sample. In continuously swept OCT systems there is limited intensity noise coming from the laser, therefore the shape of the background noise is generally low frequency and smooth. However in our system, since the laser is jumping from one mode to the next, there is a drop in power between these transitions, which cause the intensity noise seen in Figure 5-3. Because this noise is coming from the laser, it stays at a constant frequency and does not increase with fringe frequency. Thus in the image a fixed noise is expected. Because the phase of the A-line changes somewhat from one A-line to the next, it is difficult to adequately subtract this intensity noise from the fringes. However the frequency of this intensity noise will be the maximum of the baseband window bandwidth, so it will not affect the image significantly. For instance, if the A-line rate is 27 kHz, and $N_S \approx 220$ optical samples

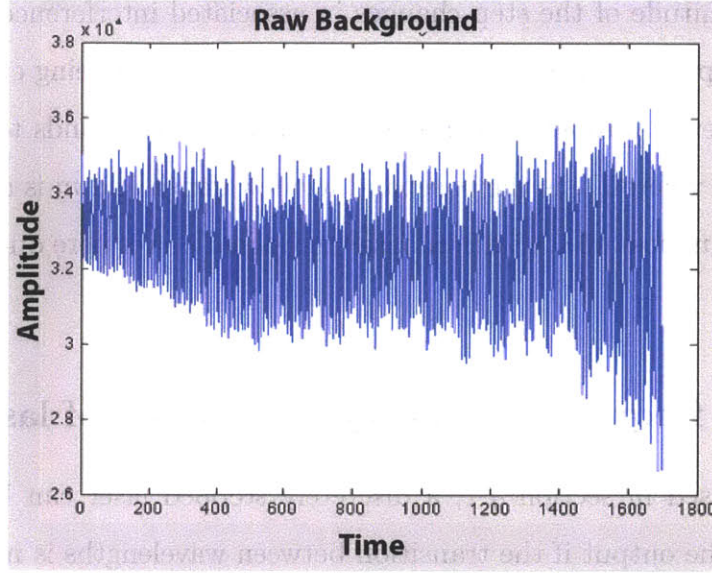


Figure 5-3: Background signal measured with sample arm blocked. High frequency intensity modulation results from unstable wavelength transition in the subsampled laser. There were 1700 points/A-line in this measurement

($N_S = \Delta\lambda / FSR \sim 100 \text{ nm} / 0.45 \text{ nm}$), then the frequency of intensity modulation is $27 \text{ kHz} \times 220 \text{ samples} \approx 6 \text{ MHz}$; the exact size of the baseband window bandwidth! Indeed the frequency of the intensity modulation was equal to $\sim 6 \text{ MHz}$ in Figure 5-1. With more careful selection of FP and/or with automatic triggering from an electro-optic OCT laser, this noise can be minimized or removed altogether.

5.3 Signal Processing

The processing protocol for imaging with the subsampled laser is outlined in Figure 5-4. A trigger pulse, which was created by sending a part of the laser of the laser output through a fiber-bragg grating (see Figure 4-6), initiated the recording of each A-line. As suggested in Figure 2-3, two galvanometer mirrors scan the tissue in a raster scan pattern in order to get traverse scans in both the x and y -directions (a.k.a. B-scan and C-scans). In many of our experiments there were 2400 points/A-line, 1024 B-scan points, and 1024 C-scan points. A-line data was saved via a C++ interface into one vector and separated in the first processing step into two channels containing

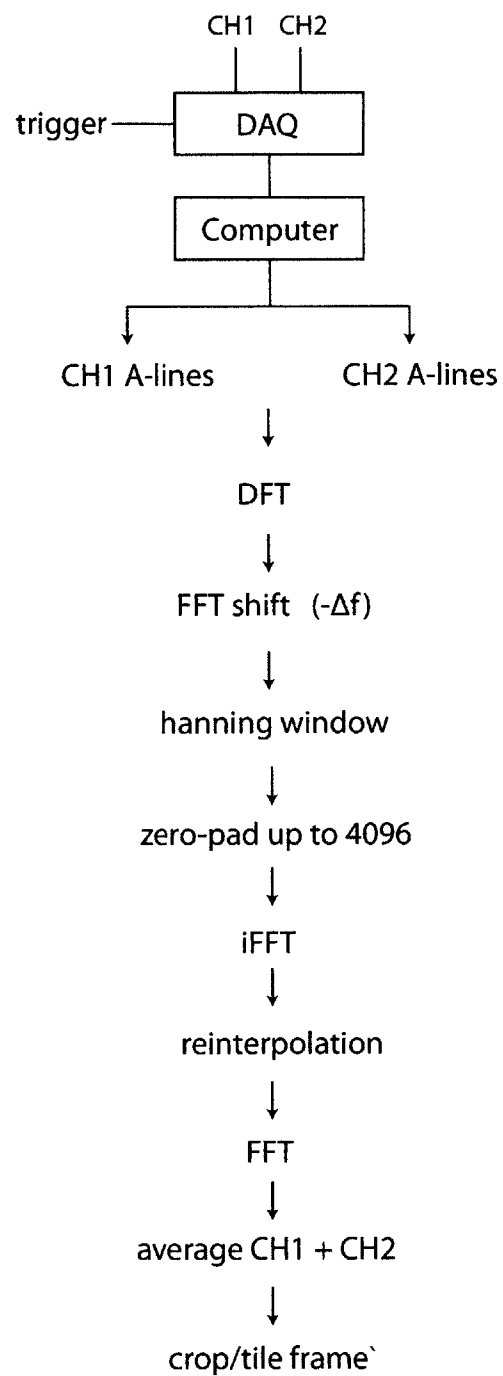


Figure 5-4: Experimental processing flowchart

a $2400 \times 1024 \times 1024$ matrix. The 2400-point DFT of each A-line was calculated and the following hanning window function was used to prevent ringing in the frequency domain [9]:

$$w_i = \frac{1}{2} \left(1 - \frac{2\pi(i-1)}{N} \right) \quad (5.1)$$

where $i = 1, 2, \dots, N$ and in our case $N = 2400$. The frequency shift of Δf that was induced by the AOFS in the interferometer (refer to Figure 2-11) was then numerically removed. The dataset was zero padded to the next power of 2 to make the interpolation and FFT step more efficient in MATLAB. If non-linearities in sampling were present, the next two steps (taking the inverse Fourier Transform and reinterpolating the dataset) linearized sampling in time to remove the effects of chirp in the laser. The mapping function is obtained by placing a mirror in the sample arm and recording fringes at two separate locations (one near path matched and one near the edge of the baseband depth) and deriving chirp from non-linearities in the phase of the FFT signal. In the final processing stage, the $4096 \times 1024 \times 1024$ matrix corresponding to each channel was averaged and cropped to remove the redundant higher order harmonic signals. The cropped images were tiled to produce a continuous image as shown in section 5.4.

5.3.1 Laser chirp in subsampled sources

Continuously swept-wavelength sources rarely sweep linearly in wavenumber-space, and thus require chirped acquisition clocks (k -clocking) or interpolation of the fringes after digitization as discussed in section 2.2.5. In optical-domain subsampling, two separate sources of laser chirp can exist; the source can be nonlinear-in- k or nonlinear-in-time (or both) as illustrated in Figure 5-5. Theoretically, optical-domain subsampling should be compatible with nonlinear-in-time chirping through either non-uniform digitizer clocking or interpolation. However, interpolation and/or clocking cannot be used to address sources that are chirped in k , i.e., which feature a varying FSR . In this case, the underlying fringes do not repeat periodically with depth, and a depth-dependent distortion is directly induced. The applications of advanced

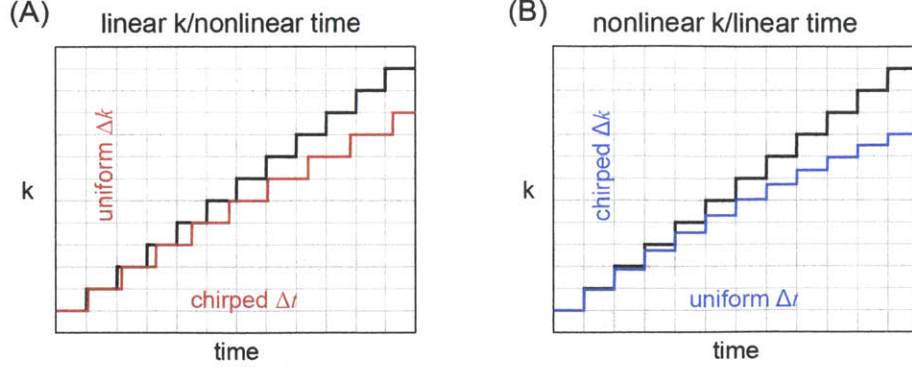


Figure 5-5: Laser chirping in optical-domain subsampled sources. A subsampled source can be chirped either in time (A) or k -space (B). In time, interpolation and/or k -clocking can be used to correct the nonlinearity. A nonlinear-in- k chirp, however, distorts the optical aliasing properties, and cannot trivially be corrected. Linear in k subsampled sources are a necessary technology to enable optical-domain subsampling.

approaches for spectral analysis of non-uniformly sampled signals may be applicable in such cases, but are beyond the scope of this work. Thus, for conventional optical-domain subsampling of bandwidth limited signals, it is important that the source have a constant FSR , but is not critical that each wavelength step occur at a fixed rate in time. Recall from equation 3.6 that the FSR is related to the the FP cavity length L and the index of refraction n :

$$FSR = \frac{c}{2nL} \quad (5.2)$$

Thus the material index n must not be dispersive over the spectral bandwidth $\Delta\lambda$ otherwise a non-linear-in- k sweep will result.

We selected our FP to have a constant FSR , so no nonlinearities in k were expected. However, because tuning of wavelengths in time was provided by the polygon laser design, non-linear-in-time chirping was expected. Recall from section 2.2.5 that the diffraction grating induces this nonlinearity in time. The higher frequency fringes are more affected by this nonlinear tuning and the width of the PSF increases as frequency increases, resulting in lower axial resolution at further depths in the tissue.

The method of removing the chirp in processing was discussed briefly in section 5.3. To confirm that a similar chirp removal algorithm is effective in a discretely sampled laser, we applied the re-interpolation to the mirror translation PSF outlined in section 5.1. A subsection of the baseband window is displayed in Figure 5-6. The original dataset (top) exhibits a signal that is broader and less intense than the de-chirped dataset (bottom). As expected, chirp is more prominent at higher frequencies (top right). De-chirping successfully narrowed the width and increased the intensity of the peak of the PSF. It should be reiterated that this chirp is an artifact of our choice of polygon-based scanning filter for this experiment; if a filter that sweeps k -space linearly in time were used, there would be no need to de-chirp the laser. Future iterations of subsampled laser should strive for linear- k sampling in order to remove this computationally expensive step.

5.4 Imaging

To validate that subsampling is applicable to OCT imaging, images of a finger and a rubber phantom were acquired with the same detection receiver outlined in Figure 4-6. The A-line rate was 27 kHz for these experiments.

5.4.1 Finger

Figure 5-7A shows the baseband window of one longitudinal cross-section of a finger. The higher order harmonic signals were cropped since they contained redundant information and were a consequence of using 100 MS/s digitizer *in lieu* of a slower digitizer. Since there was curvature in the finger, there was some discontinuity in the image due to aliasing of the tissue signal upon reaching the edge of the baseband window (arrows: location of aliasing of the surface of the sample). Interestingly, however, tiling identical copies of this baseband window lets us appreciate the continuity of the sample (Figure 5-7B). The fixed frequency noise coming from the intensity modulation of the laser can be seen in this image at the edge of the baseband window of one of the cropped cross-sections (yellow arrow). In Figure 5-7C, a depth cross

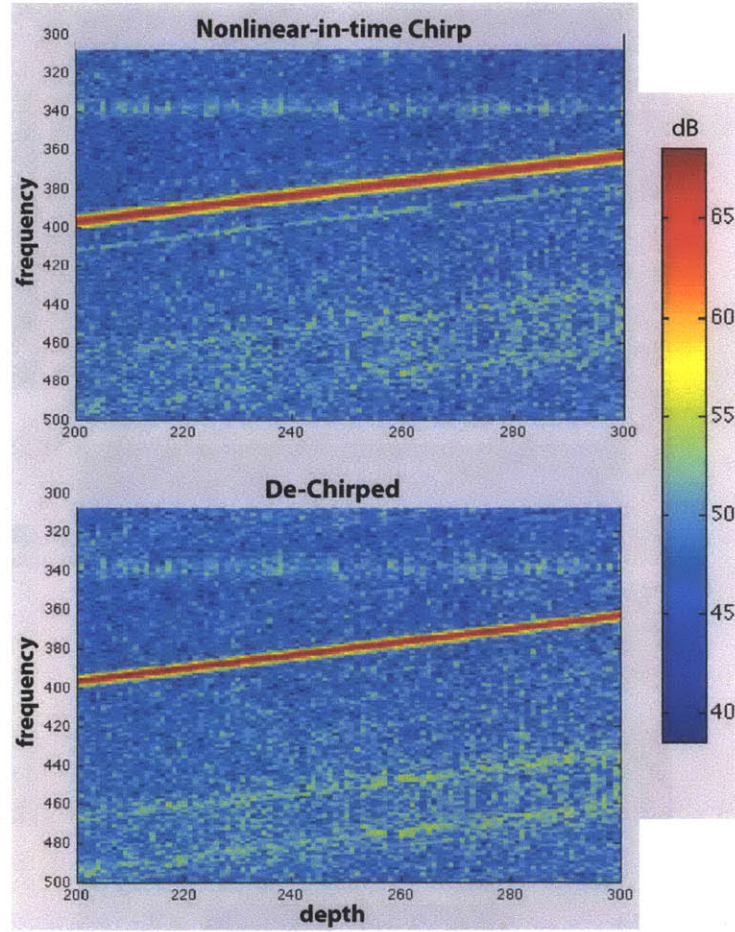


Figure 5-6: A subsection of the *imagesc* plot of the mirror translation experiment shows the difference between chirped (top) and de-chirped (bottom) signals. The width of the PSF (indicated by high intensity red signal) is reduced while the intensity is increased when the signal is de-chirped with a re-interpolation algorithm. This process increases the axial resolution of images. A 30 dB color scale is mapped here, however, the highest true intensity could be ≥ 68 dB and the lowest ≤ 38 dB.

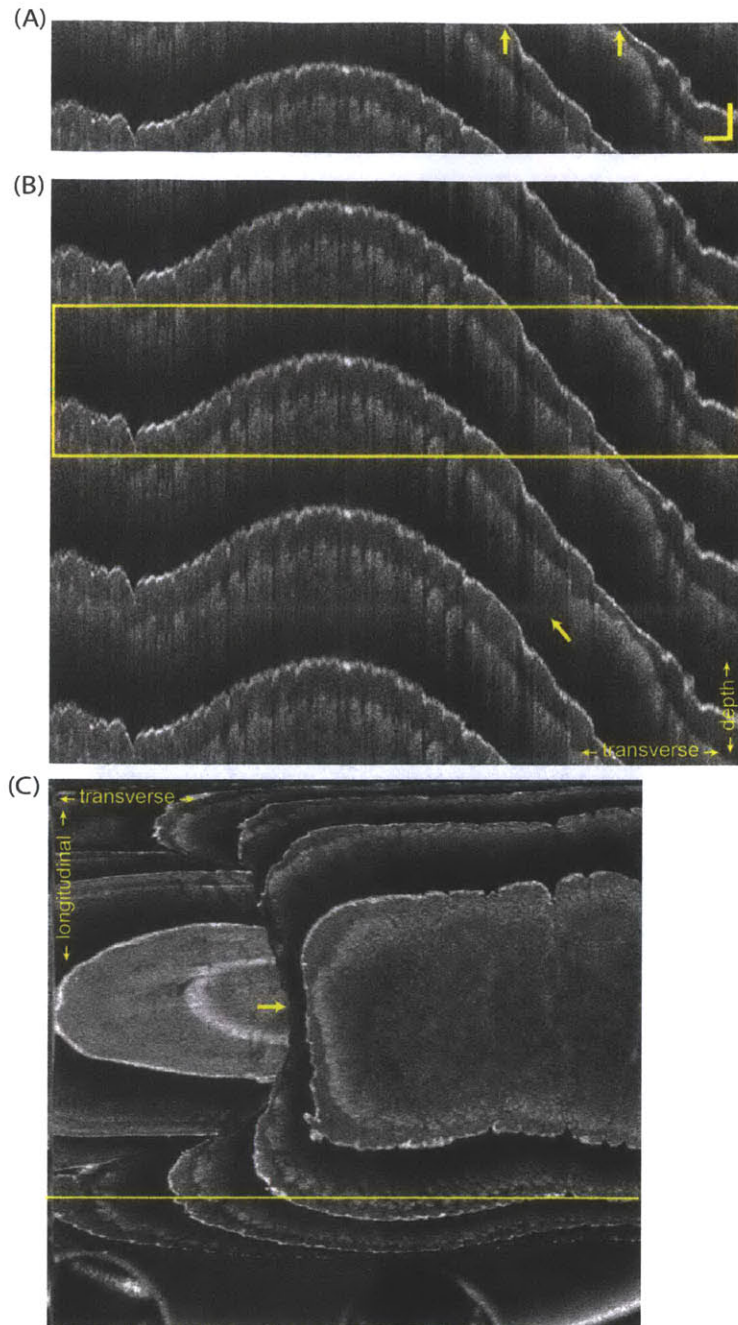


Figure 5-7: Cross-sectional images of a finger resting on a small breadboard, imaged with the subsampled OCT set-up. (A) Baseband window cross-section of the skin. Curvature of the sample causes wrapping of the surface at the location of the arrows. Scale bar: 500 μm . (B) Tiling the baseband window (outlined in yellow) allows for continuous visualization of the sample. Arrow: fixed frequency noise resulting from laser (C) En face view of the cropped/tilted image. Bar: location of longitudinal cross section in (A). Arrow: junction between the finger and the nail.

section reveals how these tiled baseband windows compile to form an *en face* image of the finger (arrow: junction between skin and finger nail). The wrapping caused by subsampling resulted in numerous depth slices being visualized in one *en face* cross-section. Theoretically, a surface finding algorithm can be employed to eliminate this effect, however, this redundant depth signals does not interfere with the interpretation of the image, and can help visualize the contour of the sample. Note that because the source *FSR* gives a ~ 1.358 mm baseband depth, the signal has fully dropped below the system noise floor before signal from the surface reappears. Because the new microscope scheme (outlined in section 4.3) was used, the B-scan and C-scan had an area of approximately 1.5 cm x 1.5 cm.

5.4.2 Rubber Phantom

The ability of subsampled OCT to support imaging over extended depth ranges is better demonstrated with a rubber phantom that is placed at a tilt so that the depth of the sample spans a range of 2 cm (Figure 5-8A). An *en face* image of this set-up shows the numerous aliased surface reflections of the rubber phantom, the metal post, and the small optical breadboard that the objects are resting on (Figure 5-8B). Since these objects were mostly opaque, the high intensity (white) signals reveal mostly the surface of the object, which have high surface reflections. Because of the tiled baseband windows, the full set-up can be interpreted from one *en face* view; this imaging paradigm has never been shown in OCT before. Notice that because of the steepness of the angle of the rubber phantom, the baseband windows appear to be closer together on the rubber, illuminating the three-dimensional contour of the set-up. Also, because the set-up was placed over 2 cm from the imaging probe a larger B-scan and C-scan area was imaged (approximately 3.5 cm x 3.5 cm). Figure 5-8C provides another *en face* image at a further depth cross-section. Although the overall set-up looks the same, the location of the surface reflections have moved slightly, meaning that in each baseband window, a different depth is being probed. Thus, subsampled imaging not only increases the ranging depth of imaging while maintaining a small acquisition bandwidth, but it can also provide

important additional information about the overall geometry of the structures that are imaged.

5.5 Subsampling in Spectrometer-Based FD-OCT

While optical-domain subsampling in this work has been described in a wavelength-swept configuration with a time-varying source, it is also applicable to spectrometer-based systems using a continuous-wave comb source. The relationship between the source FSR and the imaging window is unchanged in this configuration. In a spectrometer-based system, nonlinear-in-time chirping is replaced by nonlinear-in-pixel chirping (but may be correctable by interpolation), while nonlinear-in- k chirping remains more disruptive.

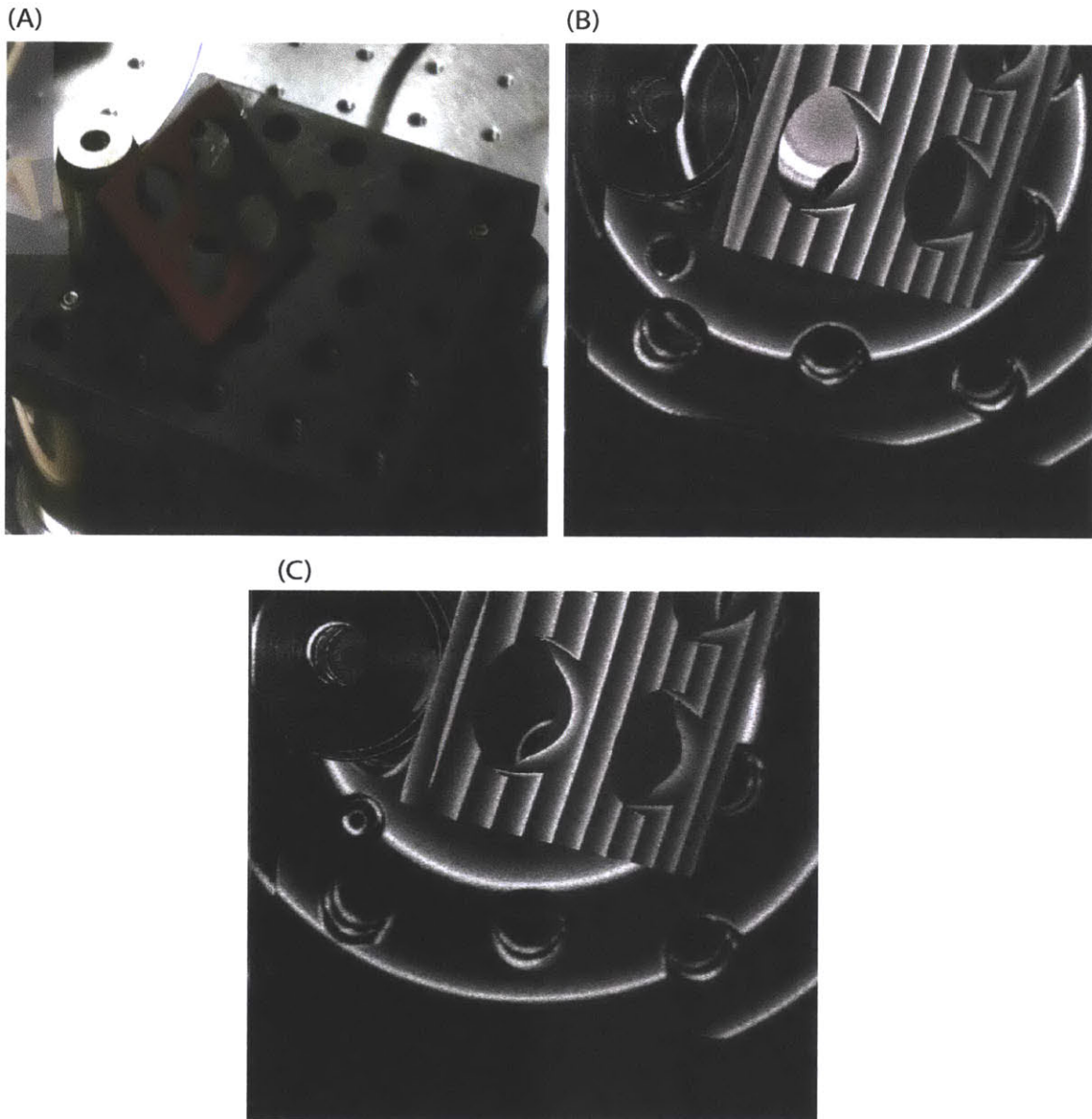


Figure 5-8: (A) Rubber phantom resting against a metal post on a small optical breadboard. The tilted rubber phantom spans 2 cm in depth. (B) An *en face* cross section of the rubber, post, and breadboard. Aliases of the tilted rubber phantom from different depth planes into this one make it possible to visualize numerous surface reflections. (C) An *en face* cross-section from another depth results in displacement of the high intensity surface reflections (white)

Chapter 6

Conclusion

6.1 Summary

This thesis introduces a method to fundamentally confine the bandwidths of OCT signals so that modern acquisition cards can faithfully acquire images along an extended depth range. Subsampling or bandpass sampling has been used extensively in the telecommunications field, however, until now it had not been used to lower the analog bandwidth of OCT signals. In the conventional continuously swept OCT, tissue is probed with an infinite set of wavelength samples, which results in successively higher frequency signals at further depths. In a discretely sampled OCT, however, a finite set of wavelengths are used, meaning that analog signals are limited to a maximum bandwidth (set by the wavelength sample size). This allows for pre-selection of the analog bandwidth of OCT signals, thereby assuring that the signals will not exceed a certain frequency. By reducing both the analog and digital acquisition bandwidth, the noise-equivalent bandwidth of optically subsampled signals does not exceed the tissue signal bandwidth as it would for RF subsampling. This is an important point to consider in preventing noise overlap and reduced SNR of the signals.

The most important achievement of this work is that it allows for long depth ranging while minimizing acquisition bandwidth. This takes advantage of the inherent sparsity of OCT signals, which arise from limited penetration of light into partially

transparent tissues. The first step in this work was to identify how to take advantage of this sparsity in order to avoid consuming acquisition bandwidth on non-tissue regions. In Chapter 3, the relationship between imaging parameters like total imaging range, baseband window depth, axial resolution and acquisition bandwidth, and system parameters like instantaneous linewidth, free spectral range, spectral bandwidth, and tuning rate was carefully established for a subsampled OCT system. This provided the theoretical foundation that inspired the construction and implementation of the subsampled OCT system in Chapter 4. To validate the principle of optical-domain subsampling, we constructed a prototype optically subsampled laser by inserting a free space Fabry-Perot (FP) etalon into a continuously swept polygon-based laser cavity. The etalon significantly reduced the instantaneous linewidth of the source through passive filtering and increased the coherence length of laser to ~ 7.4 cm. The subsampled laser was integrated with a dual balanced interferometer, which had a 25 MHz frequency shifter in the reference arm to provide necessary complex conjugate disambiguity. In Chapter 5, several imaging experiments validated the theory-based hypothesis that the optical subsampled system can image over longer ranges and with a confined acquisition bandwidth. A mirror translation experiment confirmed that a PSF signal over a 7.5 mm translation was successfully compressed into a ~ 1.358 mm baseband depth window with no overlap. We then imaged a finger and a rubber phantom to demonstrate that subsampling can be incorporated in a fully functional OCT imaging system. We took advantage of the larger imaging ranges afforded by subsampled OCT to experiment with larger field-of-view microscope designs. The ensuing images were cropped and tiled to expose the continuity of the sample. Another unexpected consequence of these cropped and tiled images was that the *en face* views revealed the three dimensional contour of the sample in one depth cross-sectional plane. This is not typical of continuously sampled OCT images and could be beneficial in the context of *in vivo* imaging where surface topography is a parameter of interest.

6.2 Experimental Limitations

It should be emphasized that the system presented in this thesis was designed to provide a proof-of-principle for applying optical subsampling to data-efficiently provide depth ranging in OCT. The system was not intended for clinical use and lacked the speed and long-term stability needed to be an effective clinical imaging system. The limitations of the system are highlighted here so that future iterations of clinical subsampled systems may effectively circumvent the issues exposed by this experimental set-up.

Higher order harmonics that arise from stepped optical fringes were discussed in section 5.2.1 as a noise source that lowers SNR of signals in the baseband window. The reduction in SNR is depth dependent, meaning that signals that are closer to the high frequency edge of the baseband window are more affected by this than those near the DC. The ~ 3.8 dB decline in baseband signal power is gradual over the span of the baseband window, meaning that it does not cause distortion in the image. It does, however, resulting in a sensitivity roll-off in the baseband window. In this work, a conventional low-pass filtered digitizer (see Figure 3-8) was used, however in future subsampled systems, this sensitivity roll-off can be avoided if specialized detector circuits employing integrate and hold amplifier circuitry are used [21].

Unstable wavelength transitions in discrete sampled sources resulted in intensity modulation of the laser output power as discussed in section 5.2.2. This modulation resulted in a fixed frequency noise at the edge of the baseband window. While this did not overlap significantly with the image, it does cause a reduction in the effective size of the baseband window and somewhat affects how well tiling of cropped baseband windows align. The amount of intensity modulation can be minimized by adjusting the instantaneous bandwidth of the scanning filter to match the FSR of the selected FP etalon. In these experiments, wavelength scanning relied on the polygon filter, and adjusting the instantaneous bandwidth of the filter was difficult to do without

sacrificing other imaging parameters (such as axial resolution) because many parameters simultaneously relied on the alignment of the telescope in the scanner. Departure from using the polygon scanner for wavelength tuning could facilitate making a better match of the FP's FSR and the tuning filter's instantaneous bandwidth. Future experiments would need to be performed to identify the best ratio of $FSR/\delta f_{tuning}$ that allows for smooth transitions between wavelengths.

Another consequence of using polygon-based tuning was that re-interpolation was necessary in MATLAB to remove the effects of nonlinear-in-time laser chirp. This step slows down computation and processing of images significantly and threatens the possibility of real-time three dimensional image rendering; this could partially obviate the advantages of having a high-speed, subsampled imaging system. Fortunately, this processing bottleneck can be avoided in several ways. In their frequency comb swept laser, Tsai *et al.* used the fact that comb frequencies were separated linearly-in-time to trigger the acquisition board off of the intensity modulation of the laser. Alternatively, if a swept laser was built that was both linear-in- k and linear-in-time, then no special trigger would be necessary and the OCT signal can simply be Fourier transformed to process images.

6.3 Impact of Subsampled OCT Systems

Subsampled OCT systems can have a significant impact on clinical imaging by enabling simultaneous long-range and high-speed imaging. Long range imaging allows access to organ types (such as colon and bladder) that were not previously amenable to OCT imaging because of tight constraints on imaging range. With subsampled OCT, these organs can benefit from a novel technology that has already positively impacted many other fields of medicine. Moreover, high-speed imaging can provide real time volumetric imaging, which would have a major advantage in any clinical setting. For instance, with real-time imaging, clinicians would have immediate feedback about the quality of images and could decide during the procedure whether

re-imaging is necessary. This would prevent the need for multiple imaging sessions that increase medical costs and patient discomfort. It would also significantly reduce missed areas that could potentially be pathologic; by imaging at 10 MHz A-line rates, for example, whole volumes can be acquired in less than a second, thereby reducing motion artifacts and total imaging time.

The possibility of new imaging paradigms with simultaneous high-speed and long-range imaging is a compelling reason for using subsampled OCT systems in the clinic. Except in cases where specialized probes exist, *in vivo* OCT has largely been used as an investigational research tool in organs such as the colon and the bladder. Comprehensive imaging made possible by high-speed and long range imaging would allow for large-scale screening with OCT in these organs. It would also enable a more intuitive imaging paradigm wherein when the imaging probe is farther away from the tissue, a larger field of view (FOV) is visible at lower resolution. And when a tissue section needs closer investigation, the imaging probe is moved closer, to view that region at higher resolution. This offers the advantage of being able to screen large surface areas of the lumen, allowing the clinician to choose what areas to view in greater detail.

6.3.1 Clinical Limitations

Although it is generally beneficial to have lower acquisition bandwidth in most imaging contexts, there are some applications for which subsampled OCT would not be necessary. Low transparency tissues, such as gastrointestinal tissues, profit greatly from this technology because they have low light penetration into the tissue and as such require small baseband window depths. This implies that imaging range can be increased significantly while maintaining a small acquisition bandwidth. In more transparent tissues such as the eye, however, the baseband window needs to be quite large to prevent signal overlap. In these applications, subsampling would not provide a significant reduction in acquisition bandwidth and might not justify the added complexity of making the source subsampled.

Another practical challenge of subsampled systems is that loose particles that flow in the path of the beam would result in a signal that aliases onto the tissue in the baseband window. Because it is impossible to distinguish where along the beam path the errant signal came from, it could cause artifacts in the tissue image that are difficult to track. This would be a problem for endoscopic procedures in which fluid is used as a medium for luminal expansion and can probably be avoided if air is used as the expansion medium instead. Particles are likely to be moving in fluid while tissue signals are stable, which could help distinguish an errant signal in the baseband window. Ideally, OCT images will be taken alongside white light endoscopic images, which would also make it easier to identify random particle aliases.

6.3.2 Future Works

While this thesis lay down the groundwork for taking advantage of optical subsampling to reduce acquisition bandwidths, adoption of this technique to high-speed systems remains as a primary goal for future work. We plan to use electro-optic components to tune wavelengths rather than a spinning polygon mirror. This would serve an advantage in speed because tuning rates will not be limited by the mechanical spin rate of the polygon motor. Furthermore, an electro-optic laser can provide finer variation in the scanning filter's instantaneous linewidth, which can reduce intensity modulations in the laser output as well as allow for linear-in-time sweeping.

Bibliography

- [1] Dennis M Akos, Michael Stockmaster, James B Y Tsui, and Joe Caschera. Direct bandpass sampling of multiple distinct RF signals. *IEEE Transactions on Communications*, 47(7):983–988, 1999.
- [2] Takuji Amano, Hideaki Hiro-Oka, DongHak Choi, Hiroyuki Furukawa, Fumiyoshi Kano, Mituo Takeda, Motoi Nakanishi, Kimiya Shimizu, and Kohji Ohbayashi. Optical frequency-domain reflectometry with a rapid wavelength-scanning superstructure-grating distributed Bragg reflector laser. *Applied optics*, 44(5):808–16, February 2005.
- [3] Tomasz Bajraszewski, Maciej Wojtkowski, Maciej Szkulmowski, Anna Szkulmowska, Robert Huber, and Andrzej Kowalczyk. Improved spectral optical coherence tomography using optical frequency comb. *Optics express*, 16(6):4163–76, March 2008.
- [4] BE Bouma and GJ Tearney. *Handbook of optical coherence tomography*. Marcel Dekker, Inc., New York, 1st edition, 2002.
- [5] Mark Brezinski. *Optical Coherence Tomography: Principles and Applications*. Elsevier Inc., Oxford, U.K., 1 edition, October 2006.
- [6] Michael Choma, Marinko Sarunic, Changhuei Yang, and Joseph Izatt. Sensitivity advantage of swept source and Fourier domain optical coherence tomography. *Optics express*, 11(18):2183–9, September 2003.
- [7] Michael J Cobb, Joo Ha Hwang, Melissa P Upton, Yuchuan Chen, Brant K Oelschlager, Douglas E Wood, Michael B Kimmey, and Xingde Li. Imaging of subsquamous Barrett’s epithelium with ultrahigh-resolution optical coherence tomography: a histologic correlation study. *Gastrointestinal endoscopy*, 71(2):223–30, February 2010.
- [8] Alan J Coulson, Rodney G Vaughan, and Mark A Poletti. Frequency-Shifting Using Bandpass Sampling. *IEEE Transactions on Signal Processing*, 42(6):1556–1559, 1994.
- [9] F.J. Harris. On the use of windows for harmonic analysis with the discrete Fourier transform. *Proceedings of the IEEE*, 66(1):51–83, 1978.
- [10] Eugene Hecht. *Optics*. Addison Wesley, San Francisco, 4 edition, October 2002.

- [11] P R Herz, Y Chen, a D Aguirre, K Schneider, P Hsiung, J G Fujimoto, K Mad-den, J Schmitt, J Goodnow, and C Petersen. Micromotor endoscope catheter for in vivo, ultrahigh-resolution optical coherence tomography. *Optics letters*, 29(19):2261–3, October 2004.
- [12] David Huang, Eric A Swanson, Charles P Lin, Joel S Schuman, William G Stinson, Warren Chang, Michael R Hee, Thomas Flotte, Kenton Gregory, Car-men A Puliafito, and G Fujimoto. Optical Coherence Tomography. *Science*, 254(5035):1178–1181, 1991.
- [13] R Huber, D C Adler, V J Srinivasan, and J G Fujimoto. Fourier domain mode locking at 1050 nm for ultra-high-speed optical coherence tomography of the human retina at 236,000 axial scans per second. *Optics letters*, 32(14):2049–51, July 2007.
- [14] R Huber, M Wojtkowski, and J G Fujimoto. Fourier Domain Mode Locking (FDML): A new laser operating regime and applications for optical coherence tomography. *Optics express*, 14(8):3225–37, April 2006.
- [15] R Huber, M Wojtkowski, and J G Fujimoto. Fourier Domain Mode Locking (FDML): A new laser operating regime and applications for optical coherence tomography. *Optics express*, 14(8):3225–37, April 2006.
- [16] J.a. Izatt, M.D. Kulkarni, K. Kobayashi, and M.V. Sivak. Optical coherence tomography and microscopy in gastrointestinal tissues. *IEEE Journal of Selected Topics in Quantum Electronics*, 2(4):1017–1028, 1996.
- [17] Eun Joo Jung, Jae-Seok Park, Myung Yung Jeong, Chang-Seok Kim, Tae Joong Eom, Bong-Ahn Yu, Sangyoun Gee, Jongmin Lee, and Moon Ki Kim. Spectrally-sampled OCT for sensitivity improvement from limited optical power. *Optics express*, 16(22):17457–67, October 2008.
- [18] R Leitgeb, C Hitzenberger, and Adolf Fercher. Performance of fourier domain vs. time domain optical coherence tomography. *Optics express*, 11(8):889–94, April 2003.
- [19] W Y Oh, S H Yun, G J Tearney, and B E Bouma. 115 kHz tuning repeti-tion rate ultrahigh-speed wavelength-swept semiconductor laser. *Optics letters*, 30(23):3159–61, December 2005.
- [20] Wang-Yuhl Oh, Benjamin J Vakoc, Milen Shishkov, Guillermo J Tearney, and Brett E Bouma. 400 kHz repetition rate wavelength-swept laser and application to high-speed optical frequency domain imaging. *Optics letters*, 35(17):2919–21, September 2010.
- [21] Ye Poberezhskiy and G Poberezhskiy. Sample-and-Hold Amplifiers Performing Internal Antialiasing Filtering and their Applications in Digital Receivers. *IEEE International Symposium on Circuits and Systems*, 3(1):439–442, 2000.

- [22] Benjamin Potsaid, Vijaysekhar Jayaraman, James G. Fujimoto, James Jiang, Peter J. S. Heim, and Alex E. Cable. MEMS tunable VCSEL light source for ultrahigh speed 60kHz-1MHz axial scan rate and long range centimeter class OCT imaging. *Proceedi*, 8213:82130M–82130M–8, February 2012.
- [23] J.M. Schmitt. Optical coherence tomography (OCT): a review. *IEEE Journal of Selected Topics in Quantum Electronics*, 5(4):1205–1215, 1999.
- [24] a Sergeev, V Gelikonov, G Gelikonov, F Feldchtein, R Kuranov, N Gladkova, N Shakhova, L Snopova, a Shakhov, I Kuznetzova, a Denisenko, V Pochinko, Y Chumakov, and O Streltsova. In vivo endoscopic OCT imaging of precancer and cancer states of human mucosa. *Optics express*, 1(13):432–40, December 1997.
- [25] Michael V Sivak, Kenji Kobayashi, A Joseph, Andrew M Rollins, Richard C K Wong, Gerard A Isenberg, and Joseph Willis. High-resolution endoscopic imaging of the GI tract using optical coherence tomography. *Gastrointestinal Endoscopy*, 51(4):474–, 2000.
- [26] E a Swanson, J a Izatt, M R Hee, D Huang, C P Lin, J S Schuman, C a Puliafito, and J G Fujimoto. In vivo retinal imaging by optical coherence tomography. *Optics letters*, 18(21):1864–6, November 1993.
- [27] G J Tearney, E Brezinski, J F Southern, B E Bouma, and J G Fujimoto. Optical Biopsy in Human Urologic Tissue Using Optical Coherence Tomography. *The Journal of Urology*, 157(May):1915–1919, 1997.
- [28] G J Tearney, M E Brezinski, B E Bouma, S a Boppart, C Pitris, J F Southern, and J G Fujimoto. In vivo endoscopic optical biopsy with optical coherence tomography. *Science (New York, N.Y.)*, 276(5321):2037–9, June 1997.
- [29] Guillermo J Tearney, Sergio Waxman, Milen Shishkov, Benjamin J Vakoc, Melissa J Suter, Mark I Freilich, Adrien E Desjardins, Wang-Yul Oh, Lisa a Bartlett, Mireille Rosenberg, and Brett E Bouma. Three-dimensional coronary artery microscopy by intracoronary optical frequency domain imaging. *JACC. Cardiovascular imaging*, 1(6):752–61, November 2008.
- [30] Tsung-Han Tsai, Chao Zhou, Desmond C Adler, and James G Fujimoto. Frequency comb swept lasers. *Optics express*, 17(23):21257–70, November 2009.
- [31] B J Vakoc, S H Yun, G J Tearney, and B E Bouma. Elimination of depth degeneracy in optical frequency-domain imaging through polarization-based optical demodulation. *Optics letters*, 31(3):362–4, February 2006.
- [32] Benjamin J Vakoc, Milen Shishko, Seok H Yun, Wang-yuhl Oh, Guillermo J Tearney, and Brett E Bouma. Comprehensive esophageal microscopy by using optical frequency-domain imaging (with video). *Gastrointestinal Endoscopy*, 65(6):898–905, 2007.

- [33] RG Vaughan, NL Scott, and RD White. The Theory of Bandpass Sampling. *IEEE Transactions on Signal Processing*, 39(9):1973–1984, 1991.
- [34] S Yun, G Tearney, Johannes de Boer, N Iftimia, and B Bouma. High-speed optical frequency-domain imaging. *Optics express*, 11(22):2953–63, November 2003.
- [35] S H Yun, C Boudoux, G J Tearney, and B E Bouma. High-speed wavelength-swept semiconductor laser with a polygon-scanner-based wavelength filter. *Optics letters*, 28(20):1981–3, October 2003.
- [36] Seok H Yun, Guillermo J Tearney, Benjamin J Vakoc, Milen Shishkov, Wang Y Oh, Adrien E Desjardins, Melissa J Suter, Raymond C Chan, John a Evans, Ik-Kyung Jang, Norman S Nishioka, Johannes F de Boer, and Brett E Bouma. Comprehensive volumetric optical microscopy in vivo. *Nature medicine*, 12(12):1429–33, December 2006.
- [37] Seok-Hyun Yun. Removing the depth-degeneracy in optical frequency domain imaging with frequency shifting. *Optics Express*, 22(5):629–629, July 2008.
- [38] Yonghua Zhao, Zhongping Chen, Zhihua Ding, Hongwu Ren, and J Stuart Nelson. Real-time phase-resolved functional optical coherence tomography by use of optical Hilbert transformation. *Optics letters*, 27(2):98–100, January 2002.